ANKARA YILDIRIM BEYAZIT UNIVERSITY

GRADUATE SCHOOL OF NATURAL AND APPLIED SCIENCES



DEVELOPMENT OF A TIME-DOMAIN SPECTROSCOPY SYSTEM FOR THE CHARACTERIZATION OF TERAHERTZ PHOTOCONDUCTIVE ANTENNA AND ANTENNA ARRAYS

Ph.D. Thesis by

Kholoud Elmabruk

Department of Electrical and Computer Engineering

June, 2019

ANKARA

DEVELOPMENT OF A TIME-DOMAIN SPECTROSCOPY SYSTEM FOR THE CHARACTERIZATION OF TERAHERTZ PHOTOCONDUCTIVE ANTENNA AND ANTENNA ARRAYS

A Thesis Submitted to

The Graduate School of Natural and Applied Sciences of

Ankara Yıldırım Beyazıt University

In Partial Fulfillment of the Requirements for the Degree of Doctor of Philosophy

In the Department of Electrical and Computer Engineering

by

Kholoud ELMABRUK

June, 2019

ANKARA

Ph. D. THESIS EXAMINATION RESULT FORM

We have read the thesis entitled "**DEVELOPMENT OF A TIME-DOMAIN SPECTROSCOPY SYSTEM FOR THE CHARACTERIZATION OF TERAHERTZ PHOTOCONDUCTIVE ANTENNA AND ANTENNA ARRAYS**" completed by **KHOLOUD ELMABRUK** under the supervision of **ASSOC. PROF. DR. MEHMET ÜNLÜ** and we certify that in our opinion it is fully adequate, in scope and in quality, as a thesis for the degree of Doctor of Philosophy.

Assoc. Prof. Dr. Mehmet ÜNLÜ

Supervisor

Assoc. Prof. Dr. Asaf Bahzat ŞAHIN

Jury Member

Prof. Dr. Hakan ALTAN

Jury Member

Prof. Dr. Halim Haldun GÖKTAŞ

Jury Member

Prof. Dr. Hamza KURT

Jury Member

Prof. Dr. Ergün ERASLAN

Director

Graduate School of Natural and Applied Sciences

ETHICAL DECLERATION

I hereby declare that, in this thesis which has been prepared in accordance with the Thesis Writing Manual of Graduate School of Natural and Applied Sciences,

- All data, information and documents are obtained in the framework of academic and ethical rules,
- All information, documents and assessments are presented in accordance with scientific ethics and morals,
- All the materials that have been utilized are fully cited and referenced,
- No change has been made on the utilized materials,
- All the works presented are original,

and in any contrary case of above statements, I accept to renounce all my legal rights.

Date: 2019, 18 June **Signature:**

Name & Surname: Kholoud ELMABRUK

ACKNOWLEDGMENTS

First and foremost, I would like to express my special appreciation and gratitude to my advisor, Professor Mehmet Ünlü for giving me the opportunity to be in his group. I am earnestly indebted to his patience, time, and continuous support that made my steps in the field stronger and much easier.

Second, I would like to thank my committee members; Prof. Dr. Asaf Bahzat Şahin, Prof. Dr. Hakan Altan, Prof. Dr. Halim Haldun Göktaş and Prof. Dr. Hamza Kurt for their time, comments and suggestions. I also want to offer special thanks to Prof. Dr. Asaf Bahzat Şahin for his generous explanations, and for Prof. Dr. Hakan Altan for giving me the opportunity to be in his lab.

Thanks to all TeraMEMS Research Group members, especially Kazim Demir for his effort in the antennas fabrication. I also want to express my special thanks to my friend Burcu Karagöz for all the time that we spent together.

I would especially like to offer my gratitude to my family, primarily my father and mother for their prayers. I am very thankful to my husband and sons for their patience on all my stresses. I am genuinely grateful for their generous support and love. I should also thank my sisters for their encouragement.

Finally, I would like to award my degree of Doctor of Philosophy to my grandfather's soul.

2019, 18 June **Kholoud Elmabruk**

DEVELOPMENT OF A TIME-DOMAIN SPECTROSCOPY SYSTEM FOR THE CHARACTERIZATION OF TERAHERTZ PHOTOCONDUCTIVE ANTENNA AND ANTENNA ARRAYS

ABSTRACT

The rapid growth in the terahertz technology necessitates high-performance components and systems to accomplish the expected performance of the state-of-the-art terahertz systems. Terahertz time-domain spectroscopy and imaging systems have become the most widely used technique for a wide range of applications in the terahertz band due to their unique functionalities. In these systems, photoconductive antennas and arrays are one of the most common approaches for the generation of the terahertz signals. In the last decade, photoconductive sources have shown significant progress, improving the technology level for the generation and detection of the terahertz signals. Although the efficiency of the terahertz photoconductive antennas have had some improvement, the low power level of the generated terahertz signals, which has stemmed from the low optical-to-terahertz conversion efficiency is a drawback that still faces the terahertz time-domain spectroscopy and imaging systems. Thus, these components have to be characterized for their beam or radiation properties, which are crucial for the system performance since they have a direct effect for the development of some terahertz applications, also they can further improve the performance of these components significantly.

A novel modified terahertz time-domain spectroscopy system is proposed to characterize the time-domain radiation pattern of terahertz photoconductive antennas. The proposed system resolves the radiation pattern spatially in the two major planes. The theoretical calculations for the proposed setup, which is based on the optical path difference method are presented and compared with the measurements. The proposed method gives a detailed time-domain characterization of the gallium arsenide based terahertz photoconductive antennas and beam-steering arrays. The characterized antennas are also examined in the simulation environment and the results are compared with the measured radiation patterns.

Keywords: Terahertz, photoconductive antennas, antenna arrays, radiation pattern, time-domain spectroscopy.

TERAHERTZ FOTOILETKEN ANTENLERINVE ANTEN DIZILERI KARAKTERİZASYONU İÇİN ZAMANA DAYALI SPEKTROSKOPİ SİSTEMİNİN GELİŞTİRİLMESİ

ÖZ

Terahertz teknolojisindeki hızlı büyüme en yeni terahertz sistemlerinin beklenen performansı gerçekleştirmesi için yüksek performanslı bileşenleri ve sistemleri gerekli kılmaktadır. Zamana dayalı terahertz spektroskopi ve görüntüleme sistemleri benzersiz fonksiyonlara sahip oldukları için terahertz bandında geniş bir uygulama yelpazesinde en yaygın kullanılan teknik haline gelmiştir. Fotoiletken antenler ve anten dizileri bu sistemlerde terahertz sinyallerinin üretilmesinde kullanılan en yaygın yaklaşımlardan birileridir. Son on yıl içinde fotoiletken kaynaklar terahertz sinyalinin üretimi ve tespiti için teknoloji düzeyini geliştirerek önemli ilerleme göstermiştir. Her ne kadar terahertz fotoiletken antenlerin verimi bir miktar gelişmiş olsada düşük optik-terahertz dönüşüm etkinliğinden kaynaklanan üretilen terahertz sinyalinin düşük güç seviyesi zamana dayalı terahertz spektroskopi ve görüntüleme sistemlerinin karşılaştığı bir sorundur. Bu nedenle, bu bileşenlerin bazı terahertz uygulamalarının geliştirilmesi için doğrudan bir etkiye sahip olduklarından sistem performansı için çok önemli olan ışın ve yayınım özellikleri açısından karakterize edilmesi gerekir. Bu, bileşenlerin performansını önemli ölçüde geliştirebilir.

Terahertz fotoiletken antenlerin zamana dayalı ışıma örüntüsü değiştirilebilen zamana dayalı terahertz spektroskopi sistemi kullanılarak araştırılmaktadır. Bu sistem ışıma örüntüsünü iki ana düzlemde uzamsal olarak çözer. Önerilen sistem için ışık yolu farkı yöntemine dayanan teorik hesaplamalar sunulmakta ve bunlar ölçümler ile karşılaştırılmaktadır. Önerilen yöntem, galyum arsenit bazlı terahertz fotoiletken antenler ve ışın demeti yönlendirme dizilerinin zamana dayalı detaylı bir karakterizasyonunu verir. Karakterize edilen antenlerin simülasyon sonuçları incelenir ve sonuçlar ölçülen ışıma örüntüsü ile karşılaştırılır.

Anahtar Kelimeler: Terahertz, fotoiletken antenler, ışın demetinin yönlendirilmesi, ışıma örüntüsü, zamana dayalı spektroskopi.

CONTENTS

Ph.D. THESIS EXAMINATION RESULT FORM ii
ETHICAL DECLARATION iii
ACKNOWLEDGMENTS iv
ABSTRACT v
ÖZ vi
NOMENCLATURE ix
LIST OF TABLES xi
LIST OF FIGURES xii

CHAPTER 1 - INTRODUCTION 1
1.1 Terahertz Radiation 1
1.2 Terahertz Radiation Properties and Applications 2
1.3 Pulsed Terahertz Generation and Detection 4
1.3.1 Nonlinear Crystals for Pulsed Terahertz Generation and Detection 5
1.3.2 Photoconductive Antennas for Pulsed Terahertz Generation and Detection 5
1.4 Research Motivations and Objectives 7
1.5 Thesis Overview 8

CHAPTER 2 - THEORETICAL BACKGROUND OF TERAHERTZ TIME-DOMAIN SPECTROSCOPY 10
2.1 Femtosecond Lasers 10
2.2 Time-Resolved Pump-Probe Technique 10
2.3 Terahertz Time-Domain Spectroscopy 12
2.3.1 Terahertz Time-domain Spectroscopy for the THz-PCA Characterizations 13
2.4 Terahertz Generation and Detection Based on Photoconductive Antennas 15
2.4.1 Generation of Pulsed Terahertz from Photoconductive Antennas 15
2.4.2 Detection of Pulsed Terahertz by Photoconductive Antennas 17
2.4.3 Substrate Lenses 18

CHAPTER 3 - THE MODIFIED THz-TDS SYSTEM 21
3.1 The Proposed Modified THz-TDS System 21
3.2 Modified THz-TDS Experimental Setup 23

3.3 THz-TDS Setup for the Characterization of the Fabricated PCAs 25
3.4 Characterized THz-PCAs and PCA Arrays 26
3.5 Conclusion 31

CHAPTER 4 - CALCULATIONS OF TIME-DOMAIN RADIATION PATTERN 32
4.1 Time-domain Representation of The Terahertz Photoconductive Antennas...32
4.2 Time-domain Representation of Terahertz Antenna Arrays 36
4.3 Simulation Setup 39
4.4 Conclusion 41

CHAPTER 5 - EXPERIMENTAL RESULTS 42
5.1 Characterization of the Fabricated THz-PCAs 42
5.1.1 Testing the THz-PCAs as THz Sources 42
5.1.2 Testing the THz-PCAs as THz Detectors.....44
5.2 Time-Domain Radiation Pattern Characterization.....45
5.3 THz Beam-Steering Array Characterization 56

CHAPTER 6 - CONCLUSIONS AND SUGGESTIONS 62
REFERENCES 64
CURRICULUM VITAE 72

NOMENCLATURE

Greek Letter Symbols

ν	Frequency
ω	Angular frequency
τ	Period
λ	Wavelength
c	Speed of light in vacuum
k	Wavenumber
h	Plank's constant
μ_0	Vacuum permeability
w_0	Spot size of the optical beam
ϕ_c	Critical emission angle of the substrate lens
ε_r	Relative dielectric constant of the lens
θ_c	Internal-incidence
η	Intrinsic impedance of the medium
ρ	Specific resistance
α	Collection angle
β	Divergence angle

Roman Letter Symbols

$I_{PC}(t_r)$	Photocurrent at the retarded time t_r
r	Distance between the observation point and the THz source
$\bar{N}$	Average electron density
R	Radius of the lens
n	Refractive index of the lens
d	Distance between the emitter and the tip of the lens
l	Dipole length
I_0	Constant
E	Electric field
H	Magnetic field
P	Observation point

h	Height
L	Virtual focus length

Acronyms

THz	Terahertz
THz-PCA	Terahertz photoconductive antenna
THz-TDS	THz time-domain spectroscopy
Tbps	Terabit-per-second
TD	Time-domain
CW	Continuous wave
EO	Electro-optic crystal
PC	Photoconductive
LT-GaAs	Low-temperature grown gallium arsenide
RD-SOS	Radiation-damaged silicon-on-sapphire
TSC	Triple stub circuit
CST	Computer Simulation Technology
fs	Femtosecond
ps	Picosecond
PDL	Polarization-dependent loss
SI-GaAs	Semi-insulating GaAs
SOS	Silicon-on-sapphire
$In_xGa_{x-1}As$	Indium gallium arsenide
HWP	Half-wave plate
CPS	Coplanar striplines
HPBW	Half-power beam width
RP	Radiation Pattern
AF	Array Factor

LIST OF TABLES

Table 1.1 Characteristic comparison between CW and TD systems 4
Table 3.1 The Summary of the characterized THz-PCAs……..29
Table 3.2 Hyper-hemispherical silicon lens specifications [69].....31
Table 4.1 The THz-PCAs representation in CST……...40

LIST OF FIGURES

Figure 1.1 Electromagnetic spectrum indicating the (THz gap)..... 1

Figure 1.2 Terahertz Applications 3

Figure 1.3 Schematic diagram of THz pulse emission from a PC antenna excited by a femtosecond laser pulse 6

Figure 1.4 Schematic representation of THz pulse detection with a PC antenna..... 6

Figure 2.1 Normalized absorption, gain spectra and lasing mechanism of a Ti:sapphire crystal [4]11

Figure 2.2 The typical time-resolved pump-probe experimental setup (BS is beam splitter, Δt is the relative time delay between the pump and probe beams [4].....12

Figure 2.3 A schematic of a typical THz-TDS setup [4] 12

Figure 2.4 THz generation from PCA [28] 15

Figure 2.5 Schematic diagram of the most commonly metal electrodes of PCA (a) dipole, (b) bow-tie and (c) stripline [60].....16

Figure 2.6 THz electric field generation by dipole PCA [4].....17

Figure 2.7 THz detection using PCAs [44] 18

Figure 2.8 (a) Substrate lens designs, ray-tracing diagrams of (b) a collimating lens and (c) a hyper-hemispherical lens [4].....20

Figure 3.1 The schematic of the modified TDS system uses for the time-domain radiation pattern characterization [66]…… 22

Figure 3.2 The calculations of the optical path difference that occurs due to the lateral movement of the detection PCA…… 23

Figure 3.3 The proposed modified THz-TDS setup implementation……. 24

Figure 3.4 The conventional THz-TDS setup implementation……. 25

Figure 3.5 The phase shifting impedance tuning TSC (a) Schematic and (b) Demonstration in HFSS [67] …… 27

Figure 3.6 Beam-steering array [68] …… 27

Figure 3.7 BATOP hyper-hemispherical Si lens (a) Photograph and (b) Schematic [69] …… 28

Figure 4.1 Finite dipole antenna (a) geometry and (b) far-field approximations [70] …… 33

Figure 4.2 Dipole antenna radiation pattern simulated in MATLAB (a) in frequency range 0.1-1 THz and (b) total radiation pattern……. 35

Figure 4.3 Dipole antenna radiation pattern simulated in HFSS (a) in frequency range 0.1-1 THz and (b) total radiation pattern……. 36

Figure 4.4 2×1 array positioned along the z-axis (a) Geometry and (b) Far-field approximations……..…… 37

Figure 4.5 2×1 array antenna radiation pattern simulated in MATLAB (a) in frequency range 0.1-1 THz and (b) total radiation pattern…… 39

Figure 4.6 The proposed method implementation in CST environment (a) E-plane (b) the H-plane…….. 41

Figure 5.1 The THz signal generated by the fabricated bow-tie PCA and detected by the commercial dipole PCA (a) time-domain and (b) frequency-domain responses 42

Figure 5.2 The THz signal generated by the fabricated 4 pi spiral PCA and detected by the commercial dipole PCA (a) time-domain and (b) frequency-domain responses 43

Figure 5.3 The THz signal generated by the fabricated butterfly PCA and detected by the commercial dipole PCA (a) time-domain and (b) frequency-domain responses 43

Figure 5.4 The THz signal generated by the fabricated bow-tie PCA and detected by the fabricated 4 pi spiral PCA (a) time-domain and (b) frequency-domain responses 43

Figure 5.5 The THz signal generated by the fabricated butterfly PCA and detected by the fabricated 4 pi spiral PCA (a) time-domain and (b) frequency-domain responses 44

Figure 5.6 The THz signal detected by the fabricated bow-tie PCA and generated by the commercial butterfly PCA (a) time-domain and (b) frequency-domain responses 44

Figure 5.7 The THz signal detected by the fabricated 4 pi spiral PCA and generated by the commercial butterfly PCA (a) time-domain and (b) frequency-domain responses 45

Figure 5.8 The THz signal detected by the fabricated butterfly PCA and generated by the commercial butterfly PCA (a) time-domain and (b) frequency-domain responses 45

Figure 5.9 The measured and calculated the max. THz signal shifted positions of the dipole PCA for the negative (LHS) and positive (RHS) transitional stage movement directions (a) E-plane and (b) H-plane.....46

Figure 5.10 The measured and calculated the max. THz signal shifted positions of the spiral PCA for the negative (LHS) and positive (RHS) transitional stage movement directions (a) E-plane and (b) H-plane 47

Figure 5.11 The measured and calculated the max. THz signal shifted positions of the bow-tie PCA for the negative (LHS) and positive (RHS) transitional stage movement directions (a) E-plane and (b) H-plane 48

Figure 5.12 The measured and calculated the max. THz signal shifted positions of the butterfly PCA for the negative (LHS) and positive (RHS) transitional stage movement directions (a) E-plane and (b) H-plane 48

Figure 5.13 Error analysis of the max. THz signal shifted positions of the dipole PCA for the negative (LHS) and positive (RHS) movement directions (a) E-plane and (b) H-plane.....49

Figure 5.14 Error analysis of the max. THz signal shifted positions of the spiral PCA for the negative (LHS) and positive (RHS) movement directions (a) E-plane and (b) H-plane 50

Figure 5.15 Error analysis of the max. THz signal shifted positions of the bow-tie PCA for the negative (LHS) and positive (RHS) movement directions (a) E-plane and (b) H-plane 50

Figure 5.16 Error analysis of the max. THz signal shifted positions of the butterfly PCA for the negative (LHS) and positive (RHS) movement directions (a) E-plane and (b) H-plane 51

Figure 5.17 The normalized measured time-domain radiation pattern of the (a) commercial dipole, (b) spiral, (c) bow-tie and (d) butterfly characterized THz-PCAs 53

Figure 5.18 Radiation Pattern (RP) of the dipole PCA (a) E-plane and (b) H-plane 54

Figure 5.19 Radiation Pattern (RP) of the spiral PCA (a) E-plane and (b) H-plane .55

Figure 5.20 Radiation Pattern (RP) of the bow-tie PCA (a) E-plane and (b) H-plane 55

Figure 5.21 Radiation Pattern (RP) of the butterfly PCA (a) E-plane and (b) H-plane 56

Figure 5.22 Beam-steering array layout [Designed by Kazim Demir] 57

Figure 5.23 The measured and calculated the max. THz signal shifted positions of the beam-steering array for the negative (LHS) and positive (RHS) transitional stage movement directions 57

Figure 5.24 Error analysis of the max. THz signal shifted positions of the beam-steering array for the negative (LHS) and positive (RHS) movement directions 58

Figure 5.25 The normalized measured time-domain radiation pattern of the beam steering array 58

Figure 5.26 Radiation Pattern of the beam-steering array 59

Figure 5.27 Beam-steering array (a) layout [Designed by Kazim Demir] (b) photograph.....59

Figure 5.28 The measured and calculated the max. THz signal shifted positions of the beam-steering array for the negative (LHS) and positive (RHS) transitional stage movement directions 60

Figure 5.29 Error analysis of the max. THz signal shifted positions of the beam-steering array for the negative (LHS) and positive (RHS) movement directions 60

Figure 5.30 The normalized measured time-domain radiation pattern of the beam steering array 61

Figure 5.31 Radiation Pattern of the beam-steering array 61

CHAPTER 1

INTRODUCTION

1.1 Terahertz Radiation

In the electromagnetic spectrum, on the low frequencies part of the spectrum, there are the radio up to millimeter waves; on the other part, there are optical waves down to far-infrared. The frequencies in between are the region (100 GHz–30THz) represents the terahertz band (THz) as illustrated in Figure 1.1. This band also is known as T-rays, T-waves or sub-millimeter wave radiation. The most commonly used units to describe the THz radiation and their conversion at 1 THz are as follows [1-4].

Frequency (ν)	➡	1000 GHz
Angular frequency ($\omega = 2\pi\nu$)	➡	6.28 THz
Period ($\tau = 1/\nu$)	➡	1ps
Wavelength ($\lambda = c/\nu$)	➡	300 μm
Wavenumber ($k = 1/\lambda$)	➡	33.3 cm^{-1}
Photon energy ($h\nu$)	➡	4.14 meV

where c is the speed of light in vacuum, and h is Plank's constant.

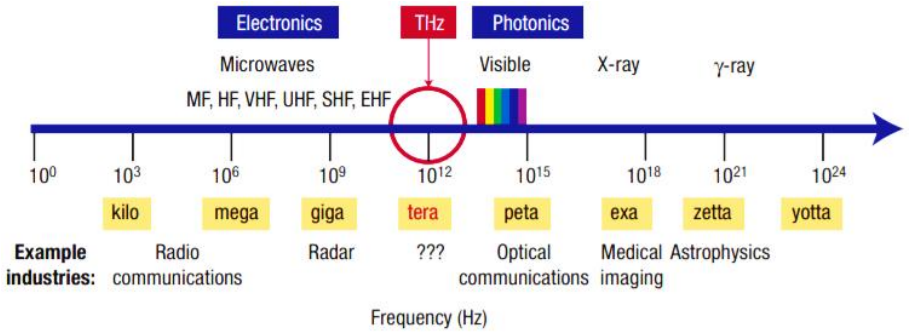


Figure 1.1 Electromagnetic spectrum indicating the (THz gap) [5]

The technical difficulties implicated in making efficient and compact THz sources and detectors led to the so-called (THz gap,) this gap has been diminishing rapidly in the last 30 years due to the tremendous development in both optical and microwave technologies [6]. The position that THz band has supplies a switch between electronics and photonics which gives a possibility to generate THz radiation using both avenues [7,8]. The rapid development in both micromachining techniques and optoelectronic devices also the advent of ultrafast lasers have given Auston et al. the opportunity to come up with the first terahertz photoconductive antenna (THz-PCA) [9]. Afterward, a novel THz generation and detection approach was developed in 1988 by Smith and co-workers with an ultra-wide measurement capability, which is the well-known THz time-domain spectroscopy (THz-TDS) [10,11].

1.2 Terahertz Radiation Properties and Applications

The location that THz radiation occupies in the electromagnetic spectrum gives it exceptional properties. THz radiation can probe the rotational transition and the vibrational modes of molecules, which provides the fingerprint of unknown components. THz radiation has low photon energy that makes it non-ionizing, and its wavelength is longer than that of the infrared waves so that it can penetrate through non-conducting materials. On the other hand, it has a shorter wavelength compared with the microwave radiation, which gives it a better spatial imaging resolution [7,8,12,13]. Moreover, it is visualized to satisfy the Terabit-per-second (Tbps) high data rate that is known as THz band communication [14]. These properties make THz radiation a key motivation for many applications in tremendous fields including biology, physics, chemistry, pharmaceutical, environmental, biomedical, communications [15,16]. Figure 1.2 represents some of these applications.

The large bandwidth available in the THz band (0.1-10 THz) makes THz communication a widely investigated application. THz radiation becomes a solution for the increasing demand to higher capacity wireless systems [14,18]. In the security scanning applications, the detection capability of THz radiation cannot be achieved using the other bands in the electromagnetic spectrum [19,20]. THz radiation can discover concealed weapons due to its ability to penetrate paper, fabrics, wood, and

plastic. This band has high information content due to its huge bandwidth, which improves spatial resolution. Moreover, many materials have unique fingerprints in this range [12,16]. The THz radiation in biomedical applications is motivated by its strong absorbance by water; predicted resonances in biomolecules; and low possibility of tissue damage due to the low energy photons [15,21]. Medical imaging application also gained an advantage over the X-rays for not damaging tissues and DNA because of this low photon energy [22,23]. THz imaging systems have safe, non-invasive, and painless detection capability of cancer tumors [16]. Moreover, these systems can differentiate between the different types of tissue in a human tooth and detect caries in the enamel layers of human teeth at an early stage [24]. In chemistry, biochemistry, and pharmaceutical industry, THz-spectroscopy systems provide novel information related to the material of interest in these fields [16].

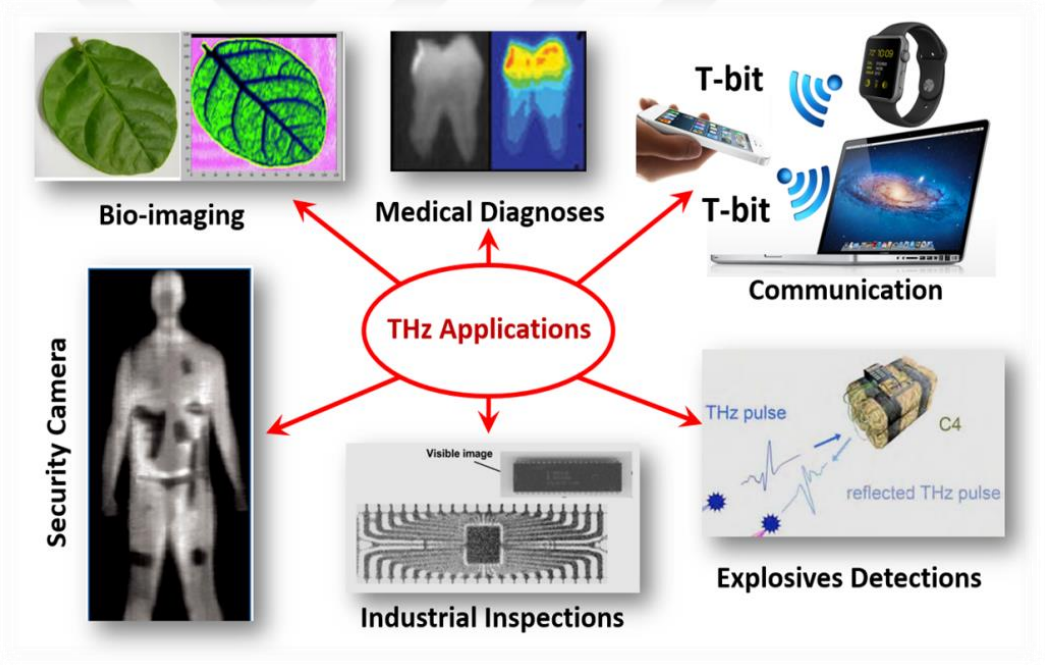


Figure 1.2 Terahertz applications [17]

THz imaging and spectroscopy systems can be designed either in pulsed (time-domain (TD)) or frequency-domain (continuous wave (CW)). In CW systems, the used THz sources are mostly developed from the electronic side where frequency multipliers generate THz signals. On the other hand, CW THz signals can be

generated from the optical side using backward-wave oscillators and quantum cascade lasers also the down-conversion by mixing two lasers working at different frequencies is possible. These systems operate at a single frequency and have a narrowband; their experimental setups are not complex. In TD systems, the optical-to-THz conversion elements namely nonlinear crystals and PCAs are the most popular for the THz generation and detection. In contrast to CW systems, the TD systems can obtain broad spectral information and coherent detection of both the amplitude and phase of each spectral component [13,20,27]. A comparison between the main features of the two systems is demonstrated in Table 1.1. This dissertation focuses on the development of pulsed systems accordingly these systems are explained in more details in chapter 2.

Table 1.1 Characteristic comparison between CW and TD systems [13]

CW Systems	*TD Systems*
➢ Narrowband	➢ Broadband
➢ High power	➢ Low power
➢ No immediate spectral data	➢ Spectral data readily
➢ Heterodyne	➢ Coherent
➢ Faster data acquisition	➢ Depth/thickness information
➢ Active and passive	➢ Active

1.3 Pulsed Terahertz Generation and Detection

Generation and detection of pulsed broadband THz radiation by means of optical-to-THz conversion namely nonlinear crystals and PCAs are the most popular in TD THz imaging and spectroscopy systems. These systems require the generation of high-power and broadband THz signals. However, the low power level of the generated THz signals of the available THz sources limits the performance of the TD systems significantly [6,28,29].

1.3.1 Nonlinear Crystals for Pulsed Terahertz Generation and Detection

THz radiation is generated using optical rectification, which is a difference frequency generation process. Nonlinear crystals with large second-order susceptibility are used in this process. Typically, utilizing optical rectification of femtosecond laser pulses incident on the electro-optic crystal (EO) are used to generate THz signals. Optical rectification occurs under specific conditions that are related to the excitation wavelength and the nonlinear material properties. Accordingly, some major factors should be considered when selecting the nonlinear crystal to generate THz signals. These factors are coherence length, absorption, and nonlinearity of the material. [11,28].

The reciprocal process of the optical rectification is EO sampling. In EO sampling, the THz signal is measured by modulating the probe laser beam inside the EO crystal. As the THz beam is incident on the crystal, it changes the refractive indices of the crystal along different axes. The phase of the linearly polarized probe beam, which is also incident on the crystal, is modulated by the refractive index changes. The changes in the polarization are converted to intensity changes that can be detected using a polarizing beam splitter or Wollaston prism and balanced photodiodes [28,29].

1.3.2 Photoconductive Antennas for Pulsed Terahertz Generation and Detection

PCAs are the electrical switch that are utilizing the increase in the electrical conductivity of semiconductors and insulators under light exposure. The fabrication of the PCA requires a short carrier lifetime, high-mobility and high-breakdown voltage material [30]. Exciting the photoconductive (PC) gap of the PCA by a laser beam, which has energy higher than the band gap energy of the PC material, generates photo-induced free carriers (electrons and holes) which generates a photo-induced current under the bias voltage. The current amplitude is a function of time

due to the laser beam pulsed nature; thus time-varying currents radiate THz waves as illustrated in Figure 1.3 [4,31,32].

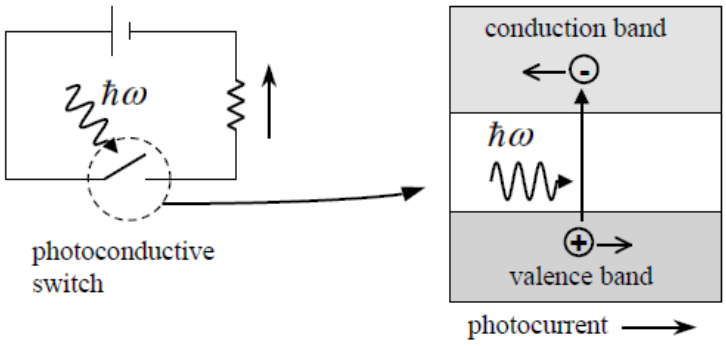


Figure 1.3 The schematic diagram of THz pulse emission from a PC antenna excited by a femtosecond laser pulse [30]

The use of the PCAs as a THz detector is similar to its use as a THz generator. The main difference is that the two electrodes of the PCA are connected to a current sensor (ammeter) to measure the photo-current generated by the probe beam across the gap under the bias of the electrical field associated with the incident THz signal as presented in Figure 1.4. The most commonly used materials in the fabrication of THz emitters and detectors are low-temperature grown gallium arsenide (LT-GaAs) and radiation-damaged-silicon-on-sapphire (RD-SOS) due to the ultra-short carrier lifetime in these materials that is caused by the high concentration of defects in which carriers are trapped and recombined [4,12].

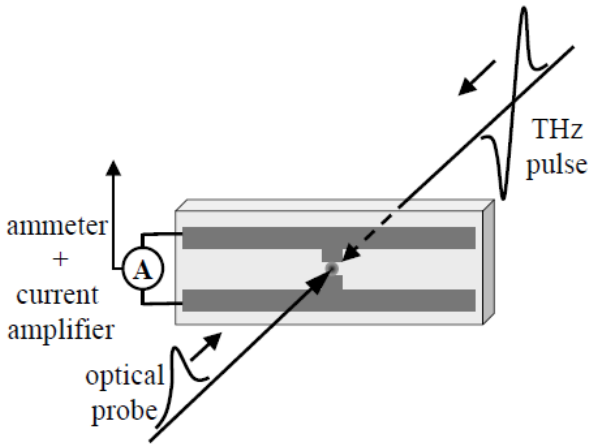


Figure 1.4 The schematic representation of THz pulse detection with a PC antenna [4]

1.4 Research Motivations and Objectives

In order to accomplish the expected performance of the state-of-the-art THz systems, high-performance components and systems are required in the progress of the THz technology. THz sources and detectors are among the most critical components of the THz systems since the generation and detection of the THz signals have a direct influence on the system level performance [3,14,21]. In the last decade, the PC sources have shown considerable progress, improving the technology level for both the generation and detection of the THz signals, that also requires the high-level characterizations of these components, not only from the perspective of the generated and detected power levels but also the spatial distribution of the generated signals [21,33,34].

THz-TDS systems since its first advent have become the most widely used technique for the characterizations in the THz region [10,11]. These systems provide a robust and stable solution due to their time-resolved nature, high signal-to-noise ratio and ability to measure both the amplitude and the phase of the transmitted, reflected and scattered THz field [15,16]. This technique has been used to investigate the THz response of several different materials, such as biological tissues, chemicals, explosives, and defect detection [5,16,21], as well as for characterizing the components that are designed for the THz band. Moreover, THz-TDS systems can be used to obtain broad spectral information and coherent detection of each spectral component in both the amplitude and phase [35,36]. These features make the THz-TDS systems a powerful tool for so many THz spectroscopy and imaging applications [22,37-39]. In these systems, a hurdle that faces these applications is the low power level of the generated THz signals, which has originated from the low optical-to-terahertz conversion efficiency [6,34,40]. Substantially, the THz-PCAs as one of the most common approaches to generate and detect the THz signals in THz-TDS systems, have been examined mostly for their generation and detection power levels, bandwidth, and noise characterizations [3,16,41]. However, the beam and radiation properties of the THz-PCAs are also needed to be characterized. These characteristics are crucial for the system performance; also, they are required due to their direct effect on the development of some novel applications namely THz

imaging, radar, and communications. Hence, the performance of the THz-TDS systems can be improved significantly by characterizing and improving the performance of the THz-PCAs [6,42].

This dissertation focuses on the development of THz-TDS systems for the characterization of THz-PCAs and beam-steering antenna arrays. The main objectives of this research can be summarized as follows:

- To design a modified THz-TDS system that characterizes the time-domain radiation pattern of THz-PCAs and antenna arrays. The proposed system spatially resolves the far-field radiation pattern of the LT-GaAs based THz-PCAs that are mounted on a Si substrate lens in the two major planes (E- and H- planes). Also,
- To characterize the beam-steering arrays utilizing the designed modified THz-TDS system. Such a characterization is performed for the first time to the best of our knowledge.
- To present the theoretical calculations for the proposed setup, based on the optical path difference method and compares the results with measurements.
- To simulate the THz-PCAs in time-domain, taking into account the Si lens effects, then comparing the simulation results with that of the measurements from the proposed setup.
- To test and characterize the designed and fabricated THz-PCAs and THz beam-steering arrays.

1.5 Thesis Overview

The dissertation is organized in five chapters. In chapter 2, the working principle of THz-TDS systems is explained. The applications of THz-TDS systems are reviewed. Furthermore, the theory of the PCAs is presented and explained.

Chapter 3 introduces the proposed modified THz-TDS system and its theoretical background. Also, illustrates the experimental setup of the proposed modified THz-TDS system and the experimental THz-TDS setup that is used to test the fabricated THz-PCAs.

Chapter 4 represents the calculations of time-domain radiation pattern and its simulation results. It also explains the implementation of the modified THz-TDS system in the Computer Simulation Technology (CST) environment [43].

Chapter 5 discusses the results of this dissertation; in the first part both the time and frequency responses of the fabricated PCAs are represented. Then, the radiation pattern characteristics of four different THz-PCAs and the beam-steering array are investigated and compared with the theoretical and numerical simulation results.

Finally, chapter 6 summarizes the work presented by this dissertation and highlights the main contributions. Subsequently, presents the challenges and suggestions for the future researches.

CHAPTER 2

THEORETICAL BACKGROUND OF TERAHERTZ TIME-DOMAIN SPECTROSCOPY

The improvement of the THz sources and detectors continue to enlarge the application areas and facilitate the switch of THz systems from the laboratory to the commercial industry. In the past decade, THz imaging and spectroscopy systems have undergone dramatic improvements. THz-TDS systems have become the most widely used powerful and stable technique to characterize materials and devices in the THz band. In this chapter, the applications, properties, the most commonly used components and the main working principle of these systems will be presented.

2.1 Femtosecond Lasers

The femtosecond (fs) laser is the laser that produces ultra-short (sub-picosecond) optical pulses using the so-called mode-locking technique. A laser with such a technique uses the active- or passive mode-locking so that a periodic train of ultra-short pulses are emitted. The dominant gain medium of femtosecond laser systems is a titanium-doped aluminum oxide (Ti:sapphire) that gives a broad spectrum ranges from 650 to 1100 nm. The four-level scheme is the lasing mechanism of a Ti:sapphire laser as illustrated in Figure 2.1, in this scheme the electrons that were excited by the green pump laser relax into lower and more stable states giving rise to a population inversion to occur that gives rise to stimulated emission near 800 nm. A Ti:sapphire laser produces 800 nm pulses of 10 to 100 fs duration at a repetition rate of approximately 80 MHz [4,12].

2.2 Time-Resolved Pump-Probe Technique

A substantial tool to study picosecond (ps) time scale ultrafast phenomena is the femtosecond lasers. The temporal resolution of ultrafast phenomena on a sub-picosecond time scale is mostly determined by the optical pulse duration. Ultra-short

optical pulses have short pulse duration, and their peak intensity can be extremely high because all of their optical energy is concentrated in such a short time. As a result of the interaction of these short and intense pulses with the material, the optical properties of the material will change. These changes originate from any of the optical excitations such as ionization, transient currents, induced polarizations, lattice vibrations, and so on [4].

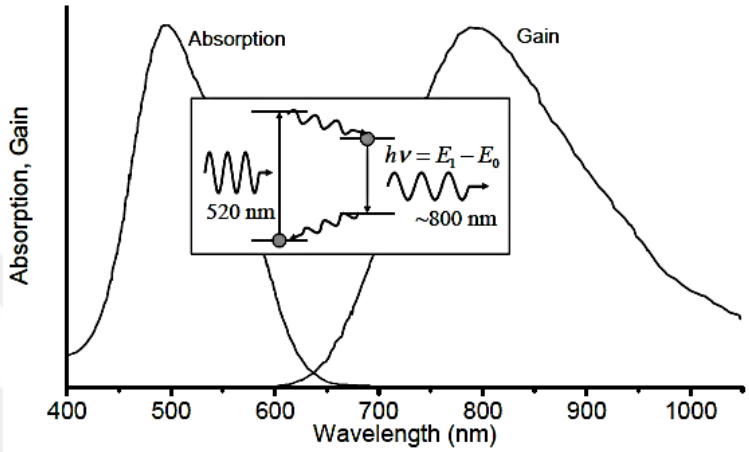


Figure 2.1 Normalized absorption, gain spectra and lasing mechanism of a Ti:sapphire crystal [4]

Pump-probe techniques are employed to investigate the transient events. The general scheme of these techniques is shown in Figure 2.2. In this technique, there is no absolute reference of time exists; the relative time delay between pump and probe pulses are used as a temporal reference frame. A beam splitter is used to split the laser beam into two to be used as a pump and probe beams. The path length of the pump line is changed using a translational stage, which adjusts the relative time delay. The pump-induced transients in the sample are analyzed by measuring probe transmission, reflectivity, and/or scattering [4,12].

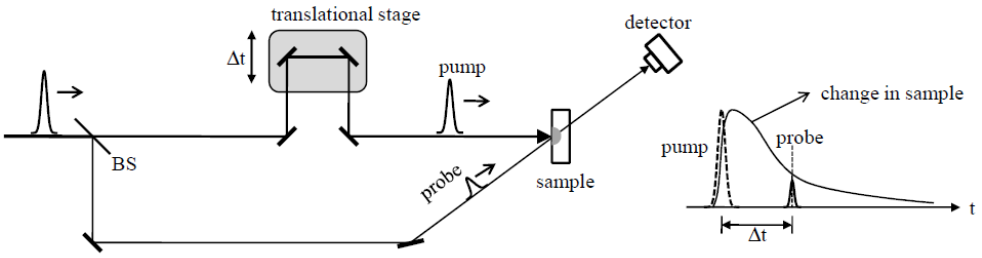


Figure 2.2 The typical time-resolved pump-probe experimental setup (BS is beam splitter, $\boldsymbol{\Delta t}$ is the relative time delay between the pump and probe beams [4]

2.3 Terahertz Time-Domain Spectroscopy

THz-TDS is based on the direct time-domain sampling with an ultrafast-laser pump/probe configuration as shown in Figure 2.3. The optical beam is split into two beams that have the same pulse duration, which is typically in the range of some femtoseconds. One of the beams, probe pulses provides the relative time delay by passing through a translational stage. Probe pulses are used to measure the THz-induced transients in the detector. The other one is the optical pump pulse that illuminates the emitter and generates the THz pulse, which travels through a distance in free space and focuses on the detector. THz pulses are generated by either transient currents or optical rectification in a photoconductive antenna or a nonlinear optical crystal respectively [4,12].

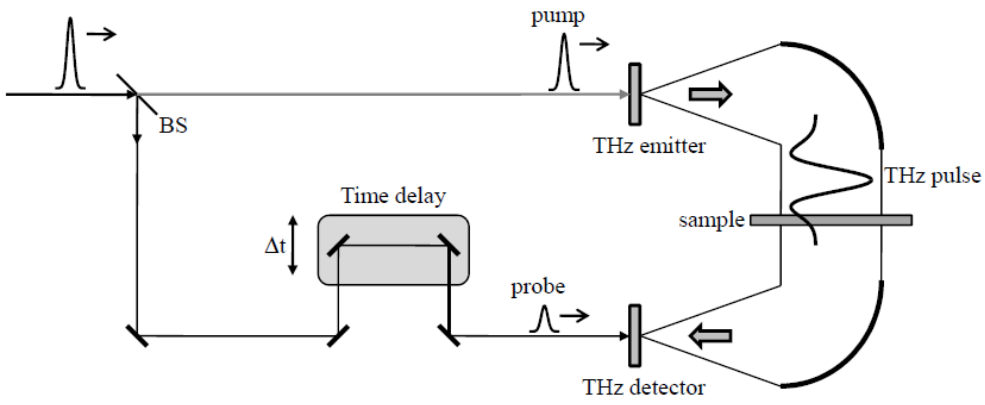


Figure 2.3 A schematic of a typical THz-TDS setup [4]

THz-TDS system uses mode-locked femtosecond lasers to produce ultra-short optical pulses. A beam splitter separates these pulses into the probe and pump beams. Typically, the pump beam has much higher energy than the probe beam since it is the beam that is used to generate the THz pulses. A time delay is employed between the pump and probe beams by changing the relative optical path between the beams utilizing a linear stage. The pump beam excites the THz source that generates electromagnetic transients (THz pulses) with a duration of few ps. The generated THz and the probe beam are aligned optically to hit the detector. Since the duration of the probe beam is much shorter than that of the THz pulse, the probe beam is considered as a delta function. Accordingly, the detected THz signal is proportional to the amplitude of the THz pulse at a specific time delay [4,44].

The THz-TDS systems have high temporal resolution since they generate THz pulses with ps pulse duration, they have large dynamics, and they are able to measure not only the amplitude, but also the phase of the transmitted, reflected, and scattered THz field systems. THz-TDS systems play a dominant role to describe the dielectric properties of sample material; also they can be used for obtaining broad spectral information and coherent detection of both the amplitude and phase of each spectral component. Additionally, in sampling the THz pulses THz-TDS systems utilize time-gating method that dramatically suppresses the background noise; thus, they have a very high signal-to-noise ratio [35,36]. These advantages make the THz-TDS systems a valuable tool for many applications in chemistry, materials sciences, engineering, pharmaceutical, spectroscopy, imaging, security, and medicine [6,35].

2.3.1 Terahertz Time-domain Spectroscopy for the THz-PCA Characterizations

THz-TDS systems have become the most commonly used technique in a wide range of THz application as a result of their unique properties [4,49]. In THz-TDS, THz-PCAs are one of the most commonly used approaches for the generation and detection of the THz signals. Although there are great improvements in the THz sources and detectors, and advances in high-speed electronics, the lack of high-power THz-PCAs is one of the challenges that faces the modern THz applications [6,34].

As the THz-TDS systems have relied extensively on the development of PCAs [6,42]; their performance can be enhanced significantly by investigating the emission properties of the PCAs. In the literature, THz-PCAs have been intensively investigated from different perspectives, mainly for their generated and detected power levels, bandwidth, and noise [3,16,41]. The effect of substrate material properties on the THz signal emission efficiency, noise, and stability for the LT-GaAs and semi-insulating GaAs (SI-GaAs) PCAs was investigated [50]. The dependency of the emission properties on the optical power and bias voltage of LT-GaAs and SI-GaAs butterfly THz-PCAs [51] also small and large aperture bow-tie THz-PCAs [52] was studied. On the other hand, the THz-TDS system was used to examine the PCAs partial polarization parameters, namely birefringence and polarization-dependent loss (PDL) [53]. A real-time THz-TDS system based on the spinning electro-optic sensor method was developed as a polarization analyzer [54]. In fact, a significant factor that can be crucial in some applications is the spatial distribution of the THz signals generated and detected by the THz-PCAs, where the pattern and the direction of the generated or detected THz beams is required [55]. The THz beam profile of an SI-GaAs PCA using aperture scanning technique [56] and PCA arrays using optical scanning [57] was investigated. These techniques utilize an indirect measurement due to the additional components used in generation and detection that results in the measurement discrepancies of the radiation properties. The photo-induced coded-aperture imaging (PI-CAI) technique was used to characterize the E- and H- planes radiation patterns of diagonal horn antenna at specific frequencies in [58]. Another study presented by Jepsen *et al*. investigated the emission distribution of an H-shaped dipole PCA on silicon on sapphire (SOS) substrate [59]. Although the characterizations were taken in a THz-TDS setup, only the radiation pattern of the PCA at specific frequencies were investigated on one of the major emission planes, Hence, the spatial emission distribution of the other types of THz-PCAs is needed to be investigated in more details for both the source and detector modes for the operation for the state-of-the-art THz-TDS systems to be more accurate.

2.4 Terahertz Generation and Detection Based on Photoconductive Antennas

Today's one of the most commonly used THz sources as well as detectors in THz-TDS systems are the THz-PCAs. A PCA consists of two metallic electrodes separated by a gap of few microns and deposited on a semiconductor substrate. The most studied and promising materials as substrates are typically a direct III-V semiconductor such as bulk GaAs, LT-GaAs, and indium gallium arsenide ($In_xGa_{x-1}As$). Broadband THz pulses can be produced from the transient photocurrent in the semiconductor substrate that is induced by the femtosecond lasers ultra-short optical pulses [4,6].

2.4.1 Generation of Pulsed Terahertz from Photoconductive Antennas

The generation of the THz pulses occurs by applying DC bias across the electrodes. Ultrafast laser pulses with photon energy larger than the semiconductor band gap generate photo-induced free carriers (free electron and hole pairs) in the gap. Then, these carriers are accelerated by the bias across the gap, and then they become trapped in the defect sites on the time scale of carrier lifetimes. This process produces photocurrent, which is the source of the sub-picosecond pulses of THz radiation. Figure 2.4 illustrates the generation of THz signals [12,32].

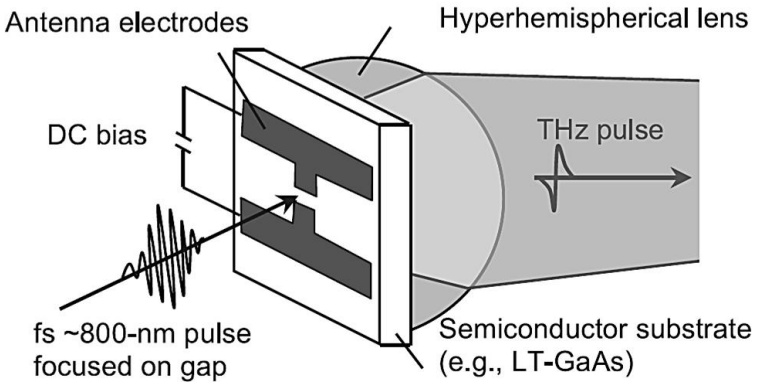


Figure 2.4 The THz generation from PCA [28]

The power and bandwidth of the generated THz signals are affected by its metal electrode structure. The most commonly used electrode structures are the stripline, dipole, and bowtie as illustrated in Figure 2.5. A THz-PCA can be modeled as a Hertzian dipole antenna. Since the source size is much smaller than the wavelength of the THz signal, the dipole approximation is valid. For simplicity, the dipole radiation in free space is considered, thus, the THz electric field that is illustrated in Figure 2.6 can be expressed as [4]:

$$E_{THz}(t) = \frac{\mu_0 w_0}{4\pi}\frac{\sin\theta}{r}\frac{d}{dt_r}[I_{PC}(t_r)]\hat{\theta} \propto \frac{dI_{PC}(t)}{dt} \quad \textbf{(2.1)}$$

The THz electric field is proportional to the time derivative of the photocurrent produced in the gap of the PCA, where μ_0 is the vacuum permeability, w_0 represents the spot size of the optical beam, $I_{PC}(t_r)$ indicates the photocurrent at the retarded time $t_r = t - r/c$, c is the speed of light in vacuum, and r is the distance between the observation point and the THz source [4,31].

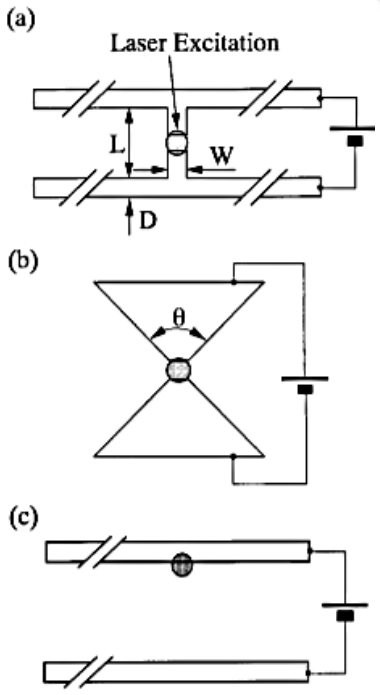


Figure 2.5 The schematic diagram of the most commonly metal electrodes of PCA (a) dipole, (b) bow-tie and (c) stripline [60]

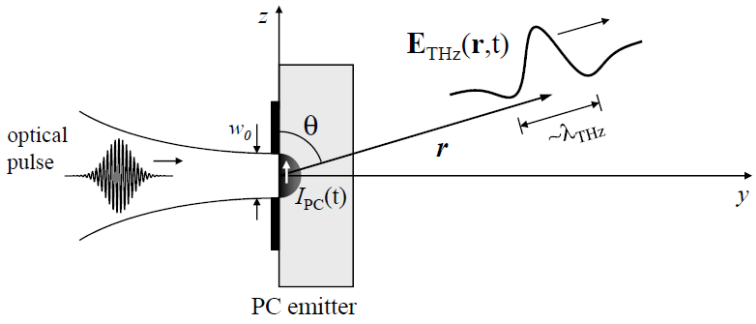


Figure 2.6 The THz electric field generation by dipole PCA [4]

The output power of the THz-PCA is affected by the optical pump power and bias voltage. The amplitude of the generated photocurrent is linearly increased by both parameters at low optical pump powers and weak bias voltage. Hence, the radiation power is expected to increase quadratically with bias and pump power. As the pump powers are further increased the field amplitude and THz output power saturates. The maximum output power that a PCA generates is limited by the breakdown voltage of its substrate material. The LT-GaAs based THz-PCAs have advantages in terms of saturation properties against optical pump power and the high breakdown voltages. Since LT-GaAs has a very high breakdown field ~500 $KVcm^{-1}$ [60] a carrier lifetime is typically about 100 to 300 fs, and reasonably good mobility ~200 $cm^2V^{-1}s^{-1}$ [61].

2.4.2 Detection of Pulsed Terahertz by Photoconductive Antennas

PCAs are widely used components for the detection of THz signal in pulsed systems. The mechanism of THz detection using PCAs is almost identical to that of THz generation via PCAs. In contrast to generation, the electrical bias is created by the electrical field of the THz pulse due to the absence of the external bias voltage. Free carriers that increase the PCA conductivity are generated in the PC gap by the optical probe pulse as shown in Figure 2.7 THz detection using PCAs [44]. Thus, a photocurrent that is directly proportional to the detected THz electric field is induced as demonstrated in. In the time domain, the THz pulse shape is detected by measuring the photo-induced current while controlling the variation in the time delay between the THz pulse and the optical probe. The THz induced photocurrent can be expressed as [4,12,44]:

$$\bar{J} \propto \bar{N} E_{THz}(\tau) \quad \textbf{(2.2)}$$

where $\bar{N}$ represents the average electron density, and τ is the temporal delay between the THz pulse and the probe pulse.

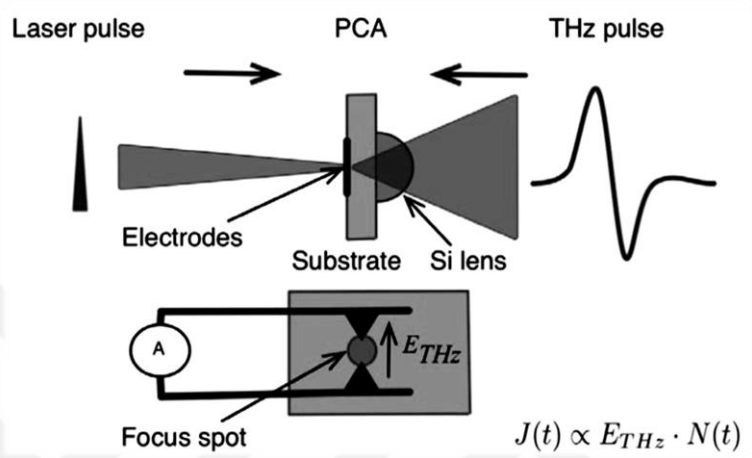


Figure 2.7 THz detection using PCAs [44]

The performance of the PCA as a detector depends on the length of the laser pulse and the carrier lifetime of the substrate material. For larger THz bandwidths, materials with shorter carrier lifetimes are required to get a sharper temporal response. The induced photocurrent is typically in the range of sub-nanoamps, thus, to convert this weak current into measurable voltages, a current amplifier is required. Moreover, a lock-in amplifier synchronized with an optical intensity modulator like an optical chopper processes the signal in order to enhance the signal-to-noise ratio [6,44].

2.4.3 Substrate Lenses

A convenient method to eliminate the total internal reflection that traps most of the generated THz radiation in the antenna substrate is to place the PCA on a dielectric lens. Since it has pioneered by Rutledge and co-workers, the substrate lenses became widely used to improve the performance of THz-TDS systems [62]. Hence, the PCA with a substrate lens tends to radiate most of its power into the lens side, which

makes the pattern of the PCA unidirectional. For dipole-type and elementary slot antennas, the power ratio between the dielectric and air is approximately $\varepsilon_r^{3/2}$, where ε_r is the relative dielectric constant of the lens. Increasing or decreasing the extension length that increases from the hyper-hemispherical length R/n can control the directivity of the substrate lens over the broad THz spectral ranges, where R is the radius and n is the refractive index of the lens, which is 3.418 for the high resistivity silicon lens [4,32,65,66]. The collimating lenses have less restriction on the bandwidth of the generated THz radiation than the hyper-hemispherical lens [62].

In the THz-TDS systems, the collimating and hyper-hemispherical substrate lenses are the most widely used lenses, which are demonstrated in Figure 2.8. The focusing ability of the lens is controlled by its shape. Accordingly, the emitter is located at the focus of the substrate lens when using the collimating lens. The emitter is located so that a minimum of the emitted rays are lost to internal reflection when using a hyper-hemispherical lens. The critical emission angle of the substrate lens can be obtained from [4,64]:

$$\phi_c = \sin^{-1}\left(\frac{R}{d-R}\sin\theta_c\right) = \sin^{-1}\left(\frac{n-1}{n}\right) \quad \textbf{(2.3)}$$

where d refers to the distance between the emitter and the tip of the lens, and θ_c represents the internal-incidence. The effective aperture size of the lens is determined by the critical angle of the total internal reflection.

For the collimating lens, the distance between the emitter (focal point) and the tip of the lens can be expressed as:

$$d_{coll} = R\left(1+\frac{1}{n-1}\right) \quad \textbf{(2.4)}$$

For the hyper-hemispherical lens, the distance between the emitter (focal point) and the tip of the lens can be expressed as:

$$d_{hyper} = R\left(1 + \frac{1}{n}\right) \quad \textbf{(2.5)}$$

For a silicon lens, the critical emission angle is 45°, $d_{coll} = 1.414R$ and $d_{hyper} = 1.293R$ [4,64].

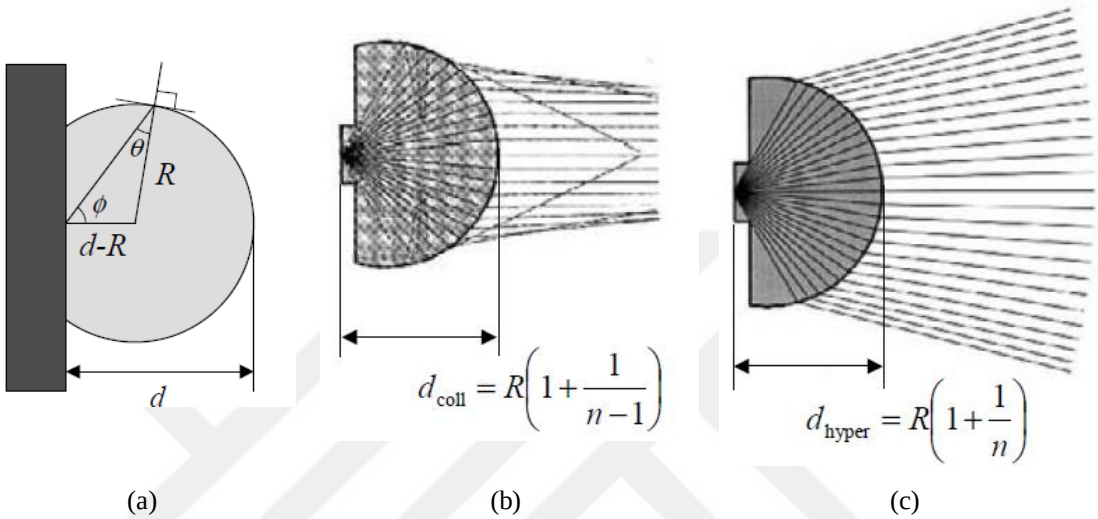


Figure 2.8 (a) Substrate lens designs, ray-tracing diagrams of (b) a collimating lens and (c) a hyper-hemispherical lens [4]

CHAPTER 3

THE MODIFIED THz-TDS SYSTEM

This chapter explains the proposed modified THz-TDS system and the experimental implementation of setup in details. As well as the implementation of the conventional THz-TDS setup that is used to test the fabricated THz-PCAs. Finally, it demonstrates the performance of the characterized PCAs.

3.1 The Proposed Modified THz-TDS System

A new technique for characterizing the time-domain radiation pattern of the THz-PCA is proposed in this thesis [65,66]. This technique is designed based on the basics of physical optics and the optical path compensation principle using the delay line in the THz-TDS systems. A one-dimensional transitional stage, which allows the detection PCA to move in the range of ±60 mm that is corresponding to ±19.1°, is used. The THz signal is detected at 5mm steps, and the collected data at each point is used to plot the radiation pattern of the THz-PCA. The design of the modified THz-TDS system is demonstrated in Figure 3.1.

The radiation pattern of the THz-PCA is measured by moving the detection PCA on the translational stage in the lateral dimension. As the detection PCA moves, an optical path difference occurs between the generation and detection arms of the THz-TDS setup that is to be compensated by the optical delay line through different time delays, the maximum THz signal for each measurement point is observed at the shifts in the physical positions of the optical delay line. These shifts are calculated as:

$$\text{Shifted Pos. for Max. THz Signal (mm)} = \text{Original Pos. for Max. THz Signal (mm)} \pm \frac{x}{2} - \frac{\Delta L}{2} \quad \textbf{(3.1)}$$

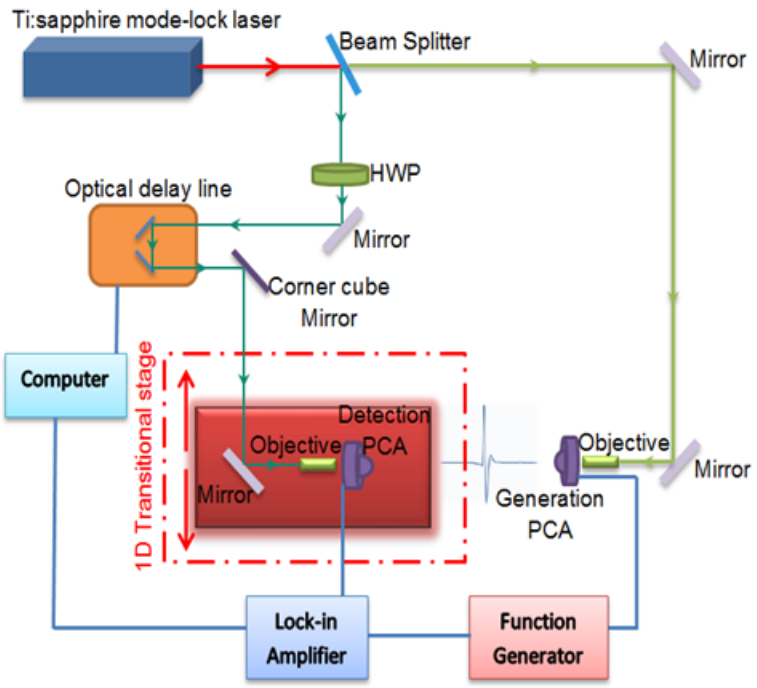


Figure 3.1 The schematic of the modified TDS system uses for the time-domain radiation pattern characterization [66]

where ± refers to the movement direction of the transitional stage, x represents the lateral position of the detection PCA, which comes from the fact that the proposed modified setup is free space, accordingly the term x does not exist in the fiber-coupled setups, and $\Delta L = \grave{L} - L$ is the optical path difference that occurs in the generation arm as demonstrated in Figure 3.2. The double path that the beam travels due to the use of the optical delay line is compensated by the term 2 in the denominator. The expected position on the optical delay line, where we get the maximum THz signal for each pattern measurement point, is found using equation (3.1).

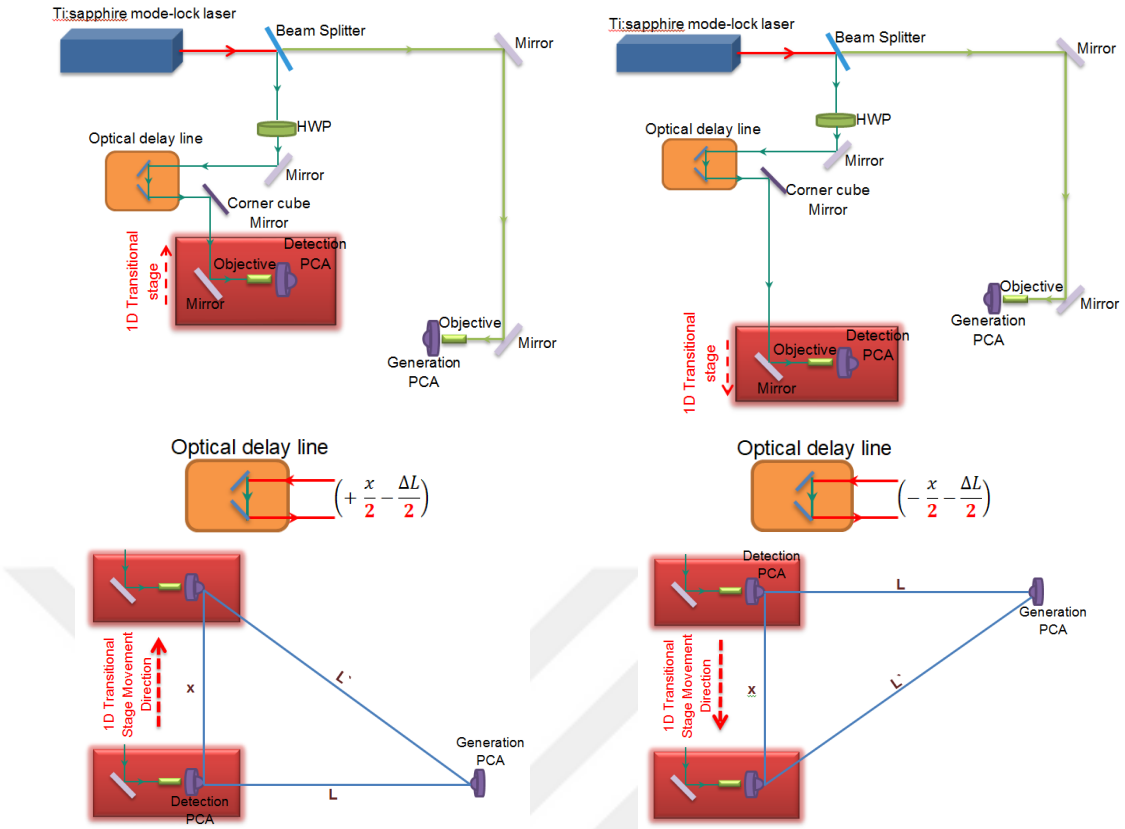


Figure 3.2 The calculations of the optical path difference that occurs due to the lateral movement of the detection PCA

3.2 Modified THz-TDS Experimental Setup

The implementation of the proposed modified THz-TDS setup is presented in Figure 3.3 [66]. This setup uses a 800nm Ti:Al_2O_3 mode-lock laser with an average output power of 300 mW, repetition rate of 75 MHz, and pulse width of 17 fs. A beam splitter divides the laser beam into two optical arms consisting of pump beam (generation arm) and probe beam (detection arm). A plane mirror directs the pump beam an attenuation filter, and then, another plane mirror directs the beam to the generation THz-PCA (antenna under test). A function generator with a 15 V bias square wave at 1 kHz give the bias to the generation PCA; the function generator is connected to a lock-in amplifier to synchronize the measurement as reference. The probe beam passes through a half-wave plate (HWP) that is used to control the polarization of the laser beam. Then, a plane mirror directs the probe beam to a computer controlled transitional stage that is used to precisely scan the path

difference between generation and detection arms. A corner cube mirror reflects the laser beam towards a plane mirror that sends it to the detection PCA. The detection PCA is fixed on a 120 mm one-dimensional transitional stage that gives the generated THz beam the opportunity to be scanned in the range of ±60 mm which corresponds to ±19.1° with respect to the position of the THz-PCA under test. The distance between the PCA under test and detection PCA is 173 mm. The off-axis THz beam error for the detection THz-PCA was investigated, where the shift of the center of the THz beam spot was found as 7.2% for the worst-case measurement point of 19.1°, which does not have a significant effect on the measurements [66].

The radiation pattern measurements in the two principal planes, namely E-plane and H-plane, are obtained by rotating both the generation and the detection PCA in the aimed plane as well as the HWP to ensure accurate results by converting the laser polarization. The collected information from the translation stage movements and lock-in amplifier is used to obtain the THz radiation pattern.

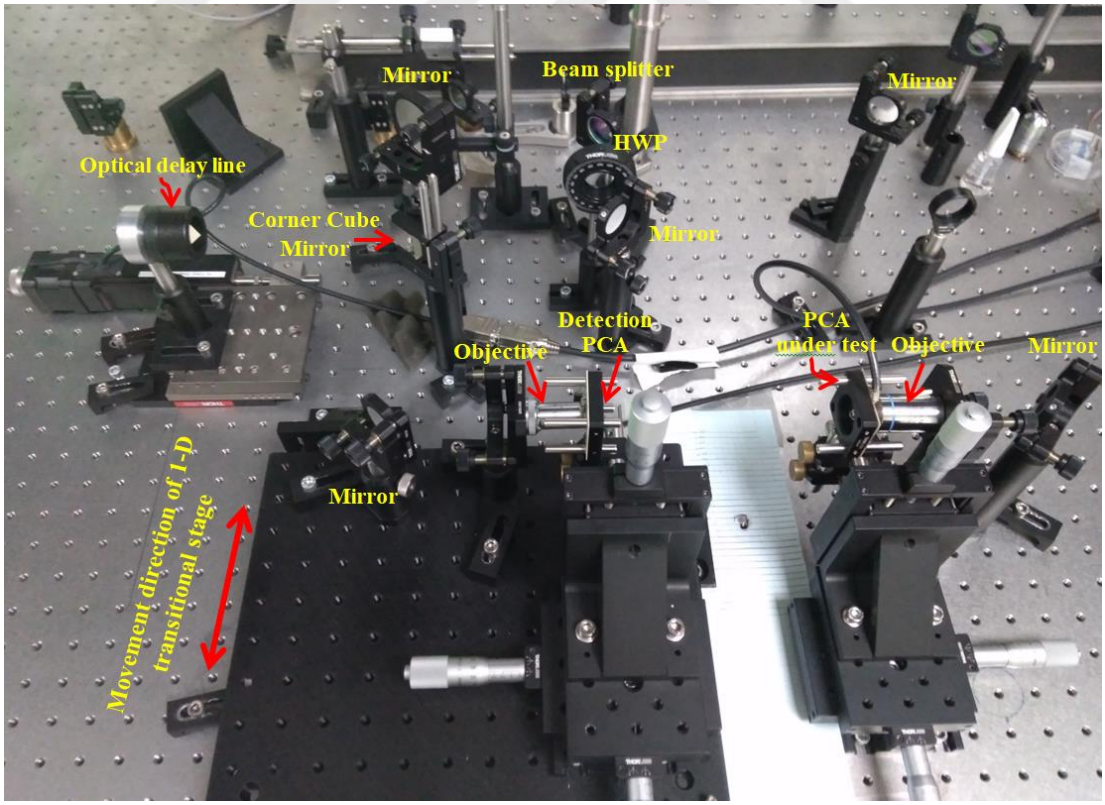
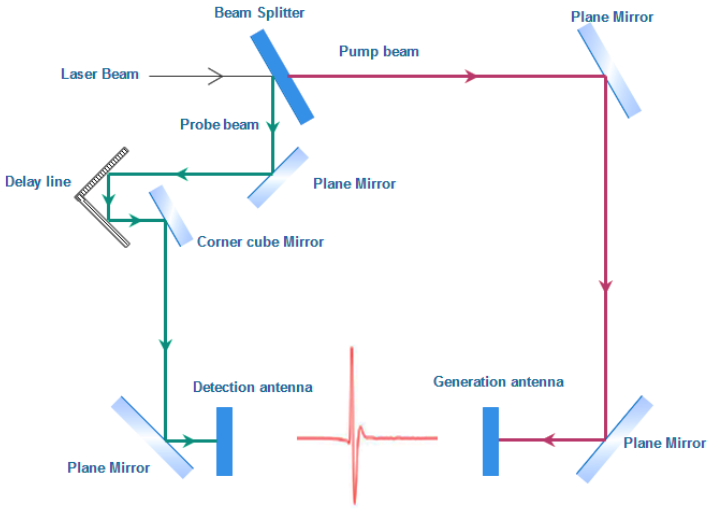


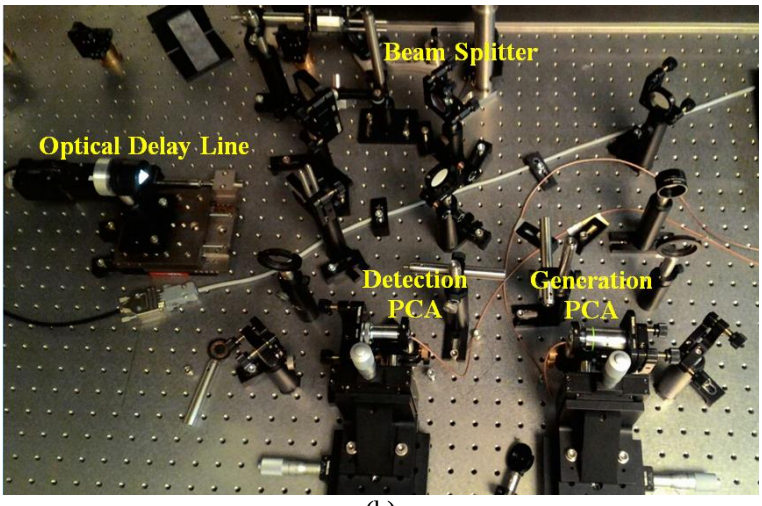
Figure 3.3 The proposed modified THz-TDS setup implementation

3.3 THz-TDS Setup for the Characterization of the Fabricated PCAs

The ability of the THz-PCAs that are designed and fabricated in our lab to generate and detect THz signal are tested in a conventional THz-TDS as illustrated in Figure 3.4. A 800nm Ti:Al_2O_3 mode-lock laser with an average output power of 300 mW, repetition rate of 75 MHz, and pulse width of 17 fs is used in this setup. The generated THz beams are detected by a THz-PCA that is fixed face to face with the generation THz-PCA.



(a)



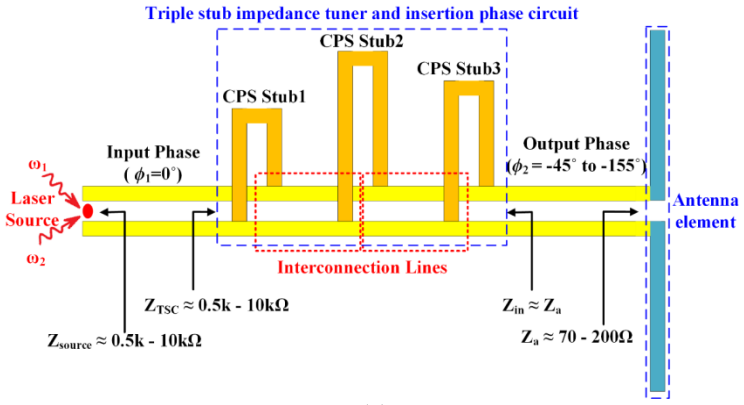
(b)

Figure 3.4 The conventional THz-TDS setup implementation

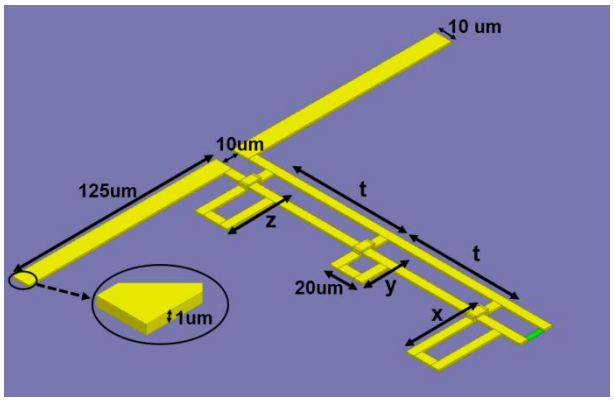
3.4 Characterized THz-PCAs and PCA Arrays

In this dissertation, the designed and fabricated THz-PCAs namely a spiral, bow-tie, and butterfly PCAs are tested as both THz generators and detectors. Then, the time-domain radiation pattern of four PCAs is measured utilizing the proposed THz-TDS setup. Two commercial PCAs namely a dipole PCA (BATOP PCA-40-05-10-800-h) and a butterfly PCA (BATOP PCA-44-06-10-800-h), the other two PCAs that were designed and fabricated in our lab namely a spiral PCA and a bow-tie PCA. A commercial dipole PCA (BATOP PCA-40-05-10-800-h) is used as a detection antenna in the proposed modified THz-TDS setup. The dimensions, materials and photographs of the packaged and integrated PCAs are given in Table 3.1.

Finally, the proposed THz-TDS setup is used to characterize the beam-steering array that is designed based on the TSC topology. The TSC, which allows the impedance tuning and insertion phase control simultaneously, is implemented using coplanar striplines (CPS) as illustrated in Figure 3.5 [67]. The characterized beam-steering array is shown in Figure 3.6 [68]. All the used THz-PCAs and the beam-steering array are mounted on a hyper-hemispherical silicon lens, which is demonstrated in Figure 3.7 and Table 3.2.



(a)



(b)

Figure 3.5 The phase shifting impedance tuning TSC (a) Schematic and (b) Demonstration in HFSS [67]

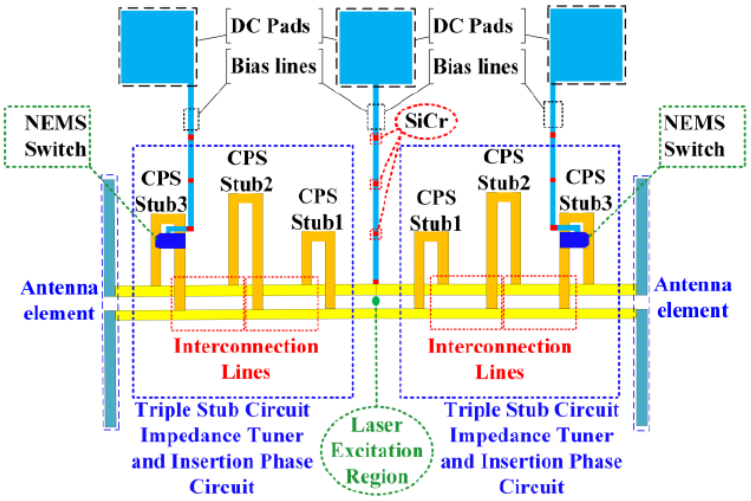
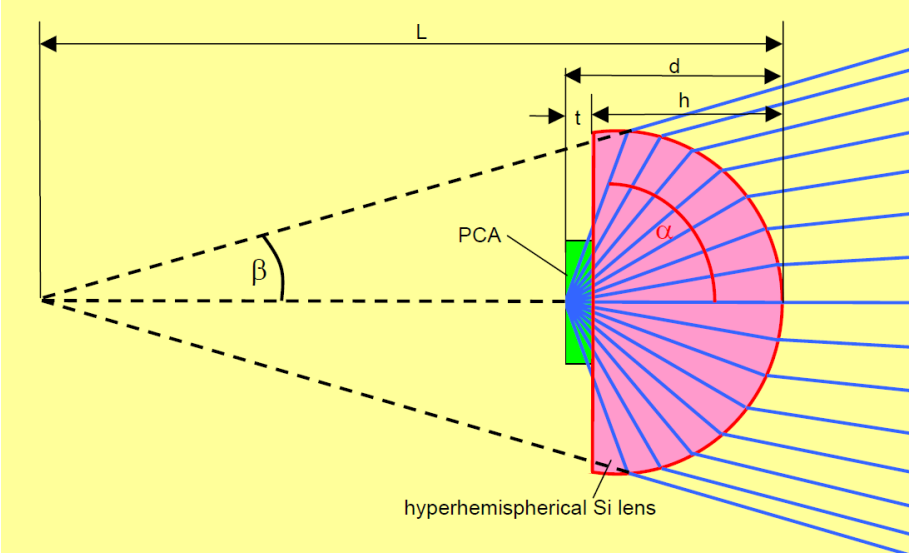


Figure 3.6 Beam-steering array [68]



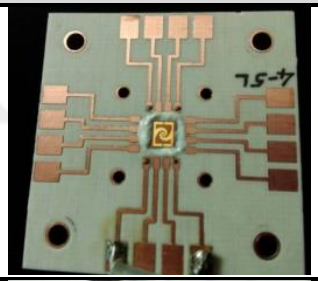
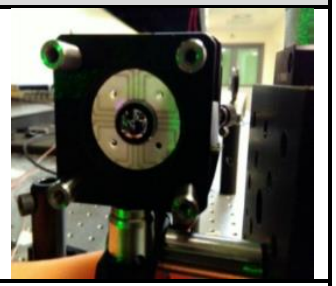
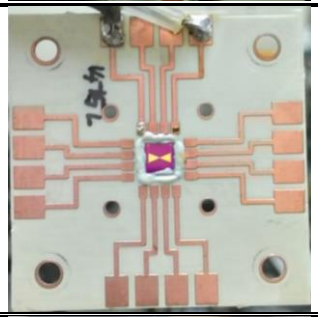
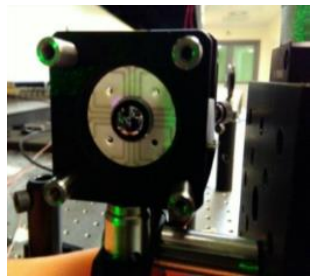
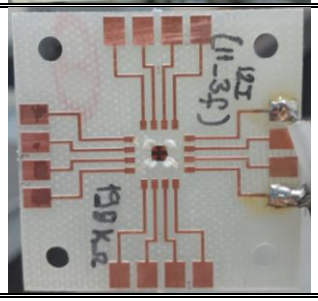
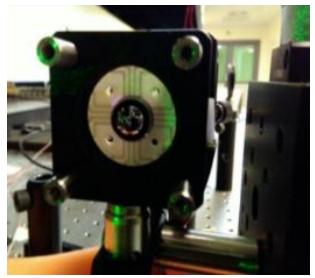
(a)

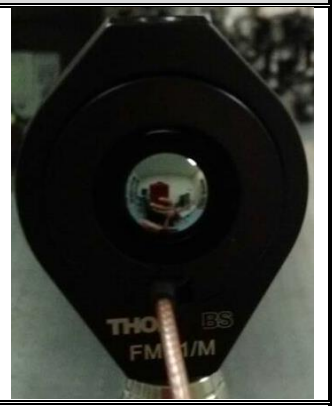


(b)

Figure 3.7 BATOP hyper-hemispherical Si lens (a) Photograph and (b) Schematic [69]

Table 3.1 The Summary of the characterized THz-PCAs

PCA Type	PCA dimensions			Substrate			Photographs	
	L “µm”	w “µm”	g “µm”	Type	Area “mm×mm”	Thickness “µm”		
Spiral	3000	4π Spiral angle	5	LT-GaAs	4×4	635		
Bow-tie	3000	10	5					
Butterfly	44	10	6		2×2	635		

PCA Type	PCA dimensions			Substrate			Photographs	
	L “μm”	w “μm”	g “μm”	Type	Area “mm×mm”	Thickness “μm”		
BATOP dipole	40	10	5	SI-GaAs	2×2	650		
BATOP butterfly	44	10	6					

* The THz-PCAs are designed and fabricated by Kazim Demir, the beam-steering array is designed by Süleymen Burak Çelik.

Table 3.2 Hyper-hemispherical silicon lens specifications [69]

Material	undoped HRFZ-silicon
Specific resistance (ρ)	>10 kΩ·cm
Refractive index (n)	3.41
Diameter	12 mm
Height (h)	7.1 mm
Distance (d)	7.7 mm
Surface	Polished
Collection angle (α)	73°
Divergence angle (β)	17°
Virtual focus length (L)	26.5 mm

3.5 Conclusion

In this chapter, the proposed modified THz-TDS setup was explained, implemented, and its theoretical calculations was illustrated. The implementation of the THz-TDS systems that was used for the fabricated THz-PCAs were demonstrated. Moreover, all the characterized THz-PCAs and PCA arrays were summarized.

CHAPTER 4

CALCULATIONS OF TIME-DOMAIN RADIATION PATTERN

This chapter presents the background and implementation of the time-domain radiation pattern calculations. Subsequently, it also explains the implementation of the modified THz-TDS system in the CST environment.

4.1 Time-domain Representation of The Terahertz Photoconductive Antennas

Dipole antennas are one of the oldest, simplest, and most versatile antennas in different areas of applications. Thus, the time-domain representation is based on a dipole operates at THz frequencies. For the mathematical complexity to be reduced a very thin dipole (ideally zero diameter) is assumed. For this representation, a very thin dipole of a finite length (*l*) that is symmetrically located about the origin and its length directed along the z-axis is used as demonstrated in Figure 4.1. Hence, the current distribution of a center-fed dipole can be expressed as [70]:

$$I_e(x'=0, y'=0, z') = \begin{cases} \hat{a}_z I_0 \sin\left[k\left(\frac{l}{2} - z'\right)\right] & , 0 \le z' \le {}^{l}/_{2} \\ \hat{a}_z I_0 \sin\left[k\left(\frac{l}{2} + z'\right)\right] & , 0 \le z' \le {}^{l}/_{2} \end{cases} \quad \textbf{(4.1)}$$

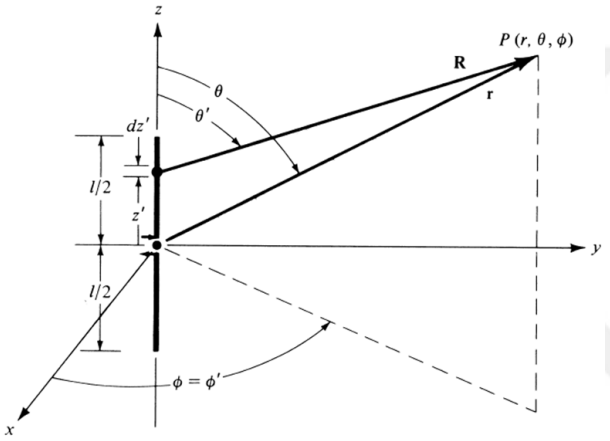
where I_0 is constant

The finite dipole antenna is subdivided into a number of infinitesimal dipoles of length $\Delta z'$. Each of the infinitesimal dipoles approaches a length of dz' by increasing the number of the subdivisions. The far-field electric and magnetic field components of an infinitesimal dipole with the given configuration are written as [70]:

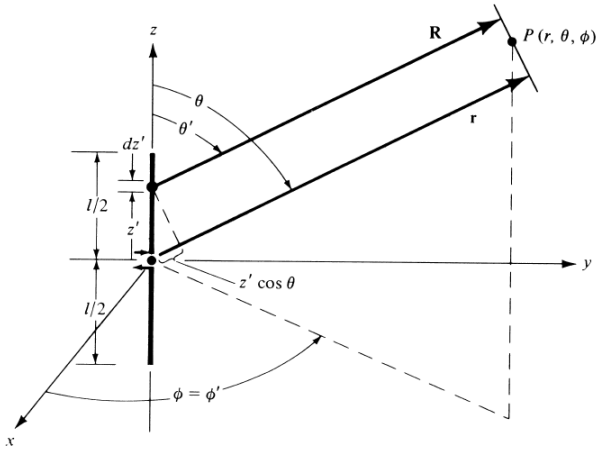
$$dE_\theta \simeq j\eta \frac{kI_e(x', y', z')}{4\pi R} e^{-jkR} \sin\theta \, dz' \tag{4.2a}$$

$$dE_r \simeq dE_\phi = dH_r = dH_\theta = 0 \tag{4.2b}$$

$$dH_\phi \simeq j \frac{kI_e(x', y', z')}{4\pi R} e^{-jkR} \sin\theta \, dz' \tag{4.2c}$$



(a)



(b)

Figure 4.1 Finite dipole antenna (a) geometry and (b) far-field approximations [70]

where η is the intrinsic impedance of the medium and R indicates the distance between any point on the source and the observation point (P) which can be written as:

$$R = \sqrt{(x-x')^2 + (y-y')^2 + (z-z')^2} = \sqrt{r^2 + (-2rz'\cos\theta\, z'^2)} \qquad \textbf{(4.3)}$$

where $r^2 = x^2 + y^2 + z^2$ and $z = r\cos\theta$. Applying the far-field approximations R becomes:

$$\begin{aligned} R &\simeq r - z'\cos\theta \quad \text{for phase term} \\ R &\simeq r \qquad\quad \text{for amplitude term} \end{aligned} \qquad \textbf{(4.4)}$$

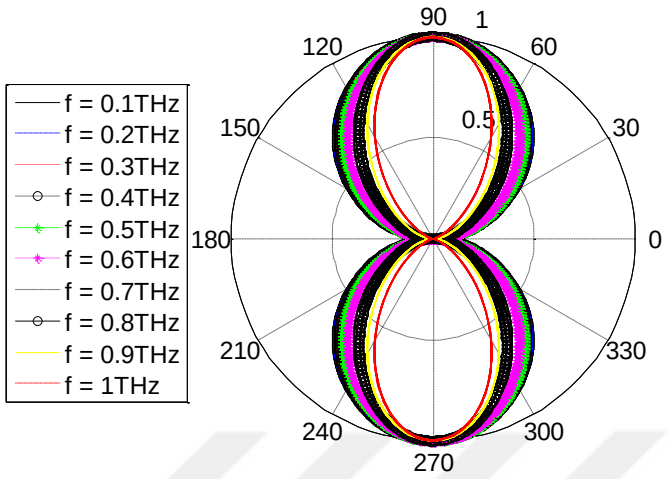
After some manipulations the total E_θ and H_ϕ components can be expressed as [70]:

$$E_\theta \simeq j\eta \frac{I_0 e^{-jkr}}{2\pi r}\left[\frac{\cos\left(\frac{kl}{2}\cos\theta\right) - \cos\left(\frac{kl}{2}\right)}{\sin\theta}\right] \qquad \textbf{(4.5a)}$$

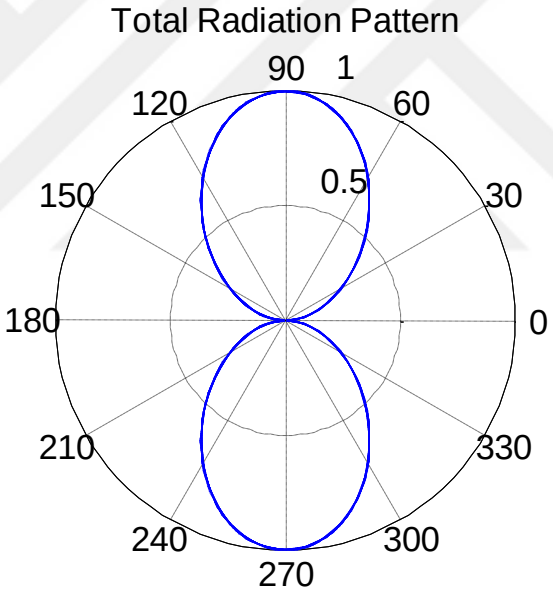
$$H_\phi \simeq \frac{E_\theta}{\eta} \simeq j\frac{I_0 e^{-jkr}}{2\pi r}\left[\frac{\cos\left(\frac{kl}{2}\cos\theta\right) - \cos\left(\frac{kl}{2}\right)}{\sin\theta}\right] \qquad \textbf{(4.5b)}$$

The transient photocurrent that is generated by the THz-PCA in the broadband THz-TDS system can be considered as the superposition of all the frequencies within the femtosecond laser source bandwidth, thus the THz pulse is generated by the coherent superposition of all the beat frequencies [35]. Accordingly, by applying equation (4.5) the radiation pattern of a dipole antenna with the length of 300 um is studied at each frequency in the range between 0.1 to 1 THz, and then the total radiation pattern is found, which represents the superposition of the radiation pattern at each frequency in the range. These radiation patterns are simulated in MATLAB [71] and

HFSS [72], and the simulated radiation patterns are demonstrated in Figure 4.2 and Figure 4.3 respectively.

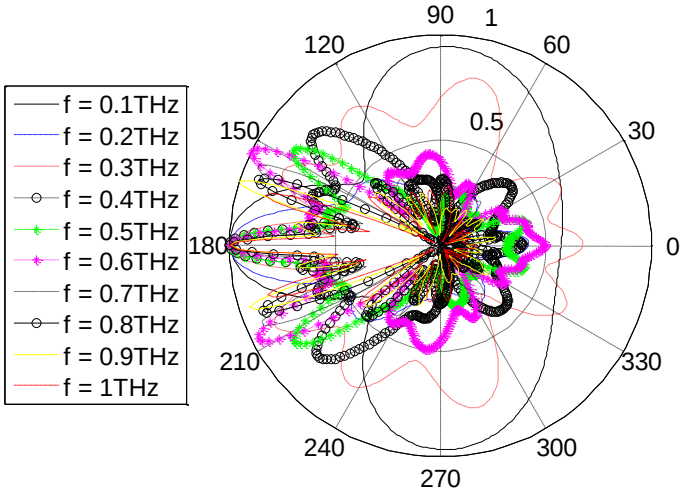


(a)

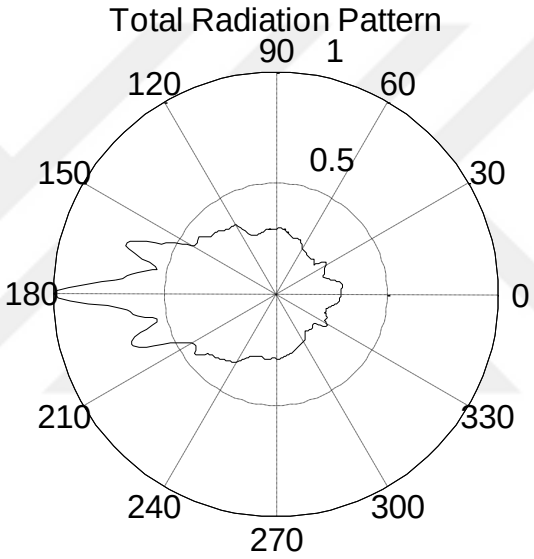


(b)

Figure 4.2 The dipole antenna radiation pattern simulated in MATLAB (a) in frequency range 0.1-1 THz and (b) total radiation pattern



(a)



(b)

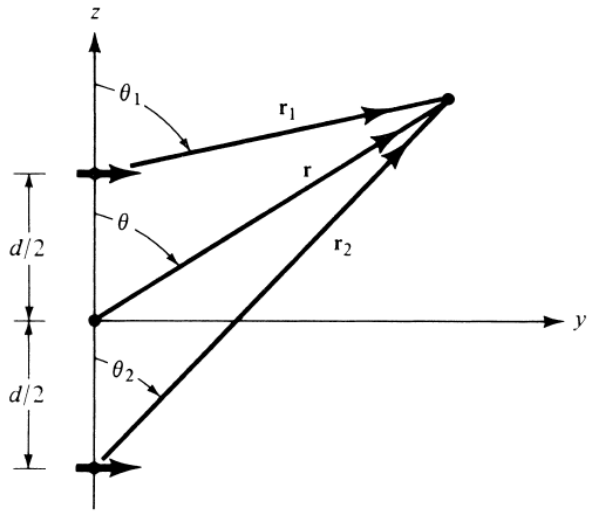
Figure 4.3 The dipole antenna radiation pattern simulated in HFSS (a) in frequency range 0.1-1 THz and (b) total radiation pattern

4.2 Time-Domain Representation of the Terahertz Antenna Arrays

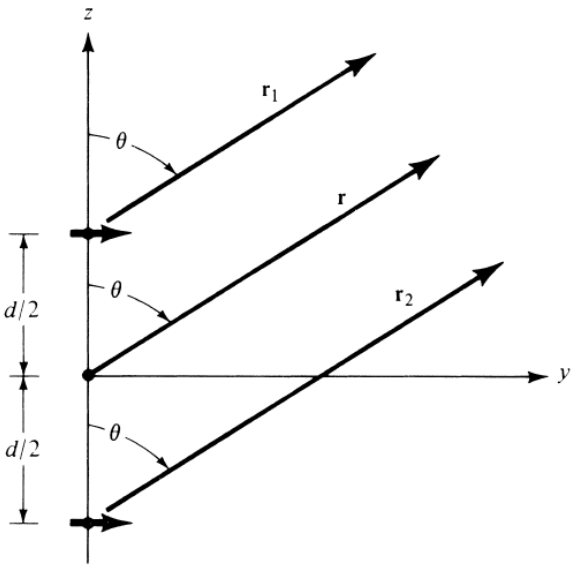
Considering an array of two infinitesimal horizontal dipoles located along the z-axis, as illustrated in Figure 4.4 (a). The total field radiated by the two elements, assuming no coupling between the elements, is equal to the sum of the two and in the y-z plane it is given by:

$$E_t = E_1 + E_2 = \hat{a}_\theta j\eta \frac{I_0 kl}{4\pi}\left[\frac{e^{-j[kr_1-(\beta/2)]}}{r_1}\cos\theta_1 + \frac{e^{-j[kr_2-(\beta/2)]}}{r_2}\cos\theta_2\right] \quad \textbf{(4.6)}$$

where β is the difference in phase excitation between the elements, where the magnitude excitation is identical.



(a)



(b)

Figure 4.4 The 2×1 array positioned along the z-axis (a) Geometry and (b) Far-field approximations

Considering the far-field approximation that is illustrated in Figure 4.4 (b),

$$\theta_1 \simeq \theta_2 \simeq \theta \tag{4.7a}$$

$$r_1 \simeq r - \frac{d}{2}\cos\theta$$

Phase variation **(4.7b)**

$$r_2 \simeq r + \frac{d}{2}\cos\theta$$

$$r_1 \simeq r_2 \simeq r$$

Amplitude variation **(4.7c)**

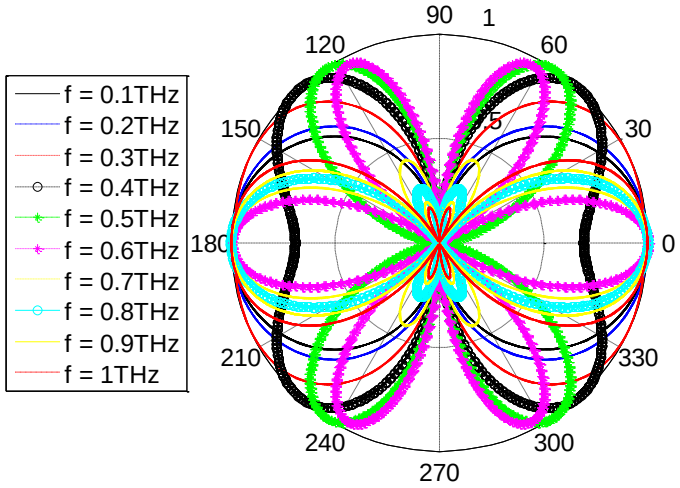
Applying the far-field condition reduces equation (4.6) to:

$$E_t = \hat{a}_\theta j\eta \frac{I_0 kle^{-jkr}}{4\pi}\cos\theta\left[2\cos\left[\frac{1}{2}(kd\cos\theta + \beta)\right]\right] \tag{4.8}$$

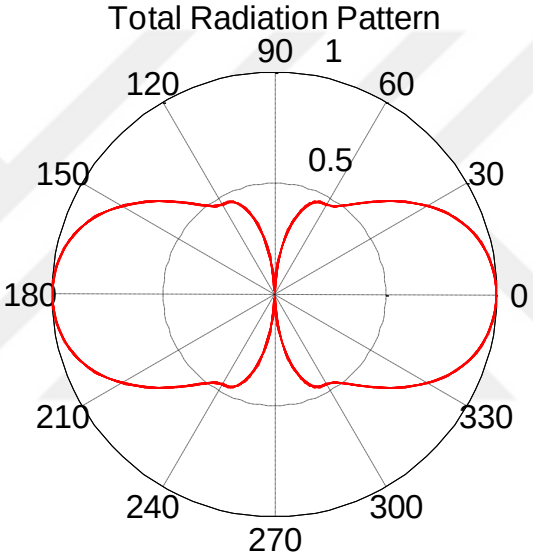
According to equation (4.8) the total radiated field of the array can be expressed as the field radiated from a single element located at the origin multiplied by the array factor (AF), which can be given for the two-element array of constant amplitude as,

$$AF = \left[2\cos\left[\frac{1}{2}(kd\cos\theta + \beta)\right]\right] \tag{4.9}$$

Accordingly, the radiation pattern of a 2×1 array based on dipole antennas, each with the length of 300 um, in the broadband frequency is simulated in MATLAB in the frequency range 0.1-1 THz. The radiation patterns at each frequency in the range are plotted in Figure 4.5 (a) and the total radiation pattern that represents the superposition of the radiation pattern at each frequency is plotted in Figure 4.5 (b).



(a)



(b)

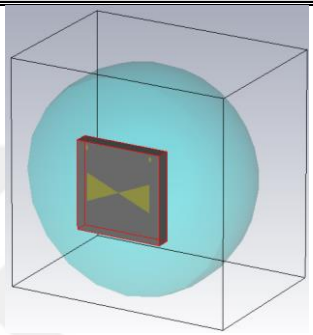
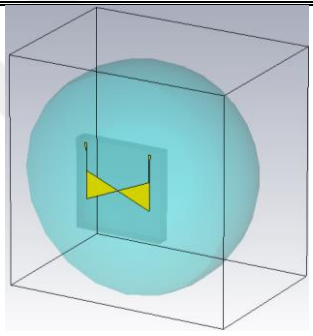
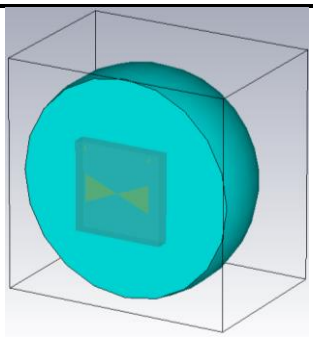
Figure 4.5 The 2×1 array antenna radiation pattern simulated in MATLAB (a) in frequency range 0.1-1 THz and (b) total radiation pattern

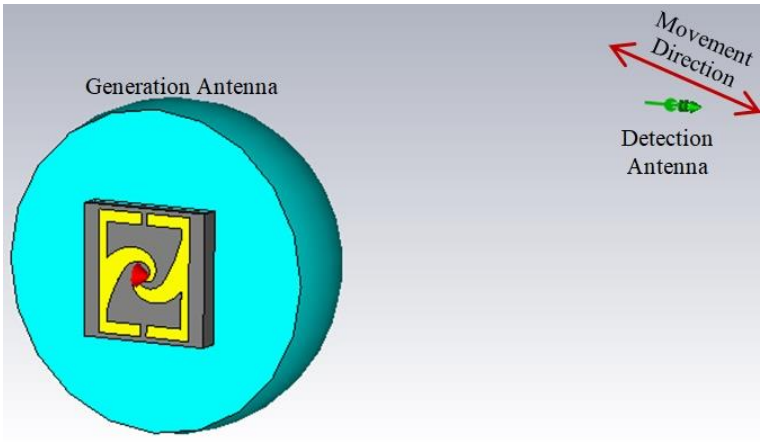
4.3 Simulation Setup

The time-domain radiation pattern of the PCAs is also examined using numerical calculations, where the commercial CST environment is used for the simulations. In the simulation environment, each THz-PCA is simulated together with a silicon lens in the time-domain as illustrated in Table 4.1, and the probe in the CST environment plays the role of the detection PCA in the proposed modified THz-TDS. The far-field time-domain radiation pattern of the each PCA is obtained by moving the probe in

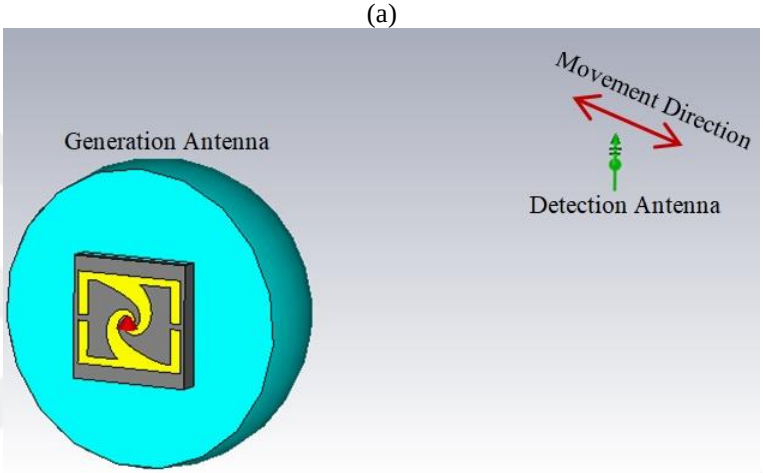
the lateral dimension, running the simulation in time-domain and recording the maximum of the time-domain signal at each measurement position in the targeted range. Figure 4.6 describes the view of the simulation setup in the CST environment for both the E- and H- plans.

Table 4.1 The THz-PCAs representation in CST

Antenna Part	Material	CST Representation
Substrate	default:import_1 Material: Gallium Arsenide (lossy) Type: Normal Epsilon: 12.94 Mu: 1 Electric tand: 0.006 (Const. fit) Rho: 5320 [kg/m^3] Thermal cond.: 54 [W/K/m] Heat capacity: 0.33 [kJ/K/kg] Diffusivity: 3.07587e-005 [m^2/s] Young's modulus: 85 [kN/mm^2] Poisson's ratio: 0.31 Thermal expan.: 5.8 [1e-6/K]	
Electrodes	default:import_3 Material: Gold Type: Lossy metal Mu: 1 Electric cond.: 4.561e+007 [S/m] Rho: 19320 [kg/m^3] Thermal cond.: 314 [W/K/m] Heat capacity: 0.13 [kJ/K/kg] Diffusivity: 0.00012502 [m^2/s] Young's modulus: 78 [kN/mm^2] Poisson's ratio: 0.42 Thermal expan.: 14 [1e-6/K]	
Si lens	component1:Si lens Material: HRFZ Si Type: Normal Epsilon: 11.62 Mu: 1 Electric cond.: 0.001 [S/m]	



(a)



(b)

Figure 4.6 The proposed method implementation in CST environment (a) E-plane (b) H-plane

4.4 Conclusion

In this chapter, the theoretical and numerical calculations of the THz-PCAs and PCA arrays in time-domain were represented. The fact that the THz pulse is generated by the coherent superposition of all the beat frequencies was studies. Furthermore, the proposed THz-TDS setup was simulated.

CHAPTER 5

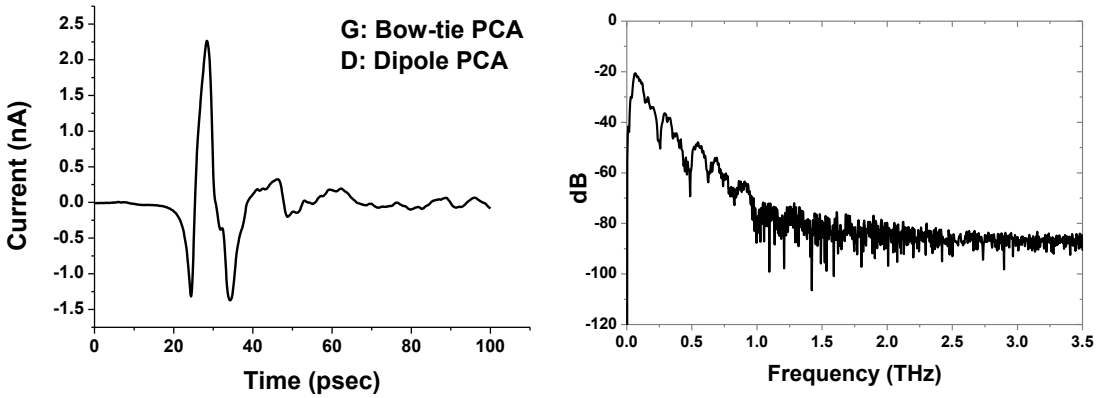
EXPERIMENTAL RESULTS

The tests of the designed and fabricated THz-PCAs are represented in this chapter. Moreover, the time-domain radiation pattern characterization of two locally fabricated as well as two commercial PCAs are discussed.

5.1 Characterization of the Fabricated THz-PCAs

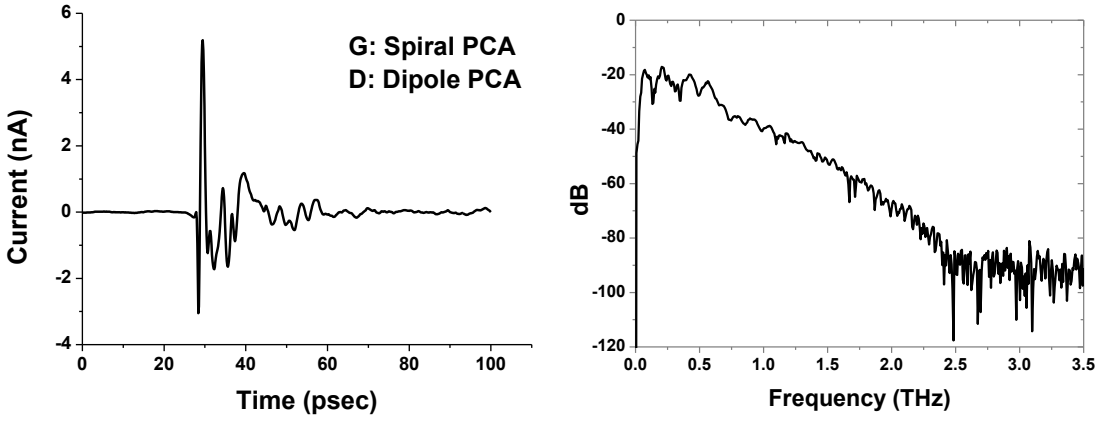
5.1.1 Testing the THz-PCAs as THz Sources

Each of the locally fabricated bow-tie, and butterfly PCAs are tested as THz sources using two different THz-PCA detectors namely the commercial BATOP dipole PCA and the local designed and fabricated spiral PCA. These detectors are narrow-band and wide-band PCAs, respectively. The locally fabricated spiral is tested as a THz source, and the generated signal is detected by the commercial dipole PCA. The responses of the generated THz signals in the time- and frequency domains are illustrated in Figure 5.1 to Figure 5.5. Thus, various types of THz-PCAs ranging from relatively narrow-band (bow-tie and butterfly) to wide band (spiral) THz-PCAs are now successfully designed and fabricated in Turkey.



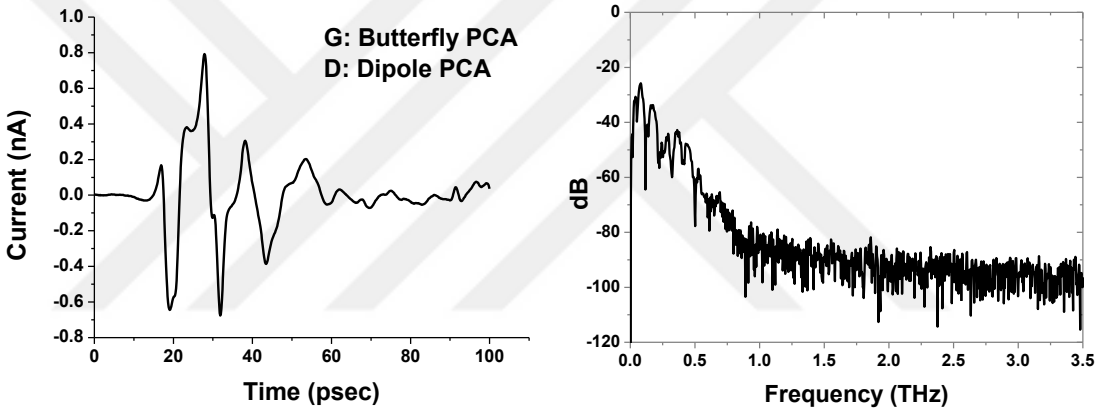
(a) (b)

Figure 5.1 The THz signal generated by the fabricated bow-tie PCA and detected by the commercial dipole PCA (a) time-domain and (b) frequency-domain responses



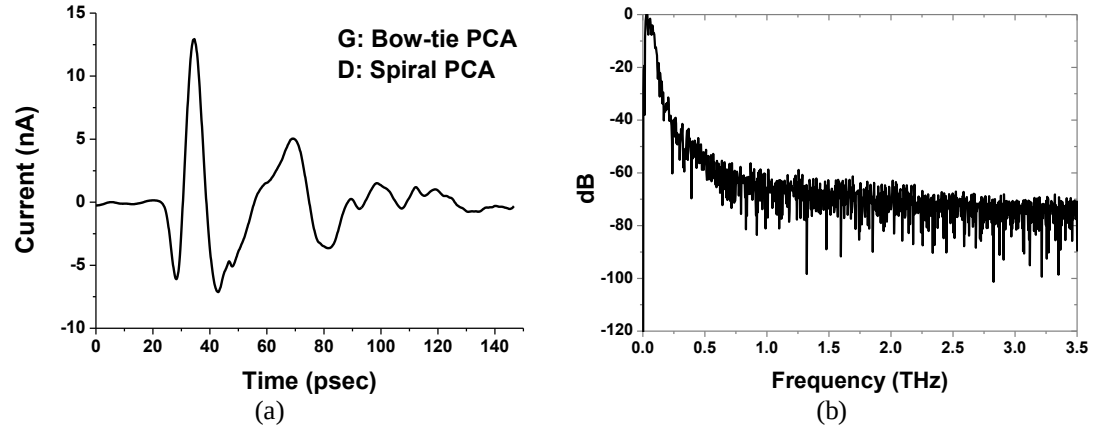
(a) (b)

Figure 5.2 The THz signal generated by the fabricated spiral PCA and detected by the commercial dipole PCA (a) time-domain and (b) frequency-domain responses



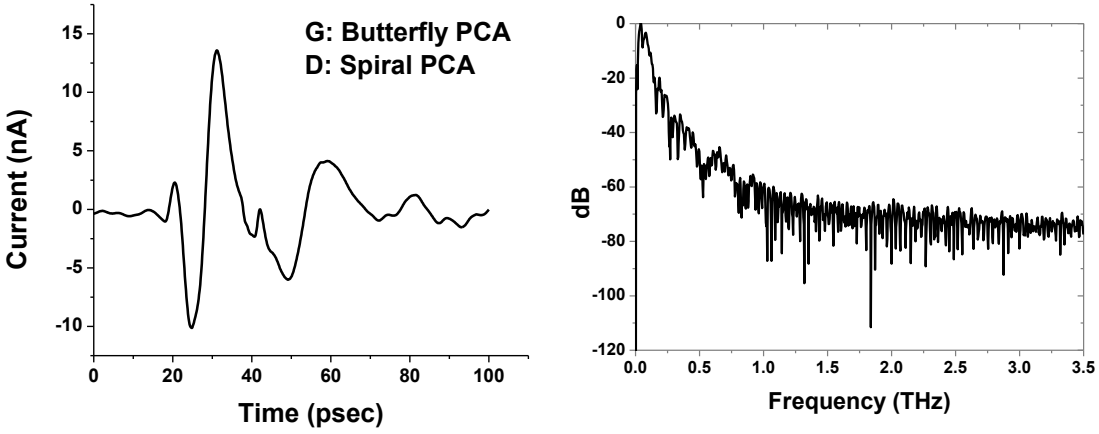
(a) (b)

Figure 5.3 The THz signal generated by the fabricated butterfly PCA and detected by the commercial dipole PCA (a) time-domain and (b) frequency-domain responses



(a) (b)

Figure 5.4 The THz signal generated by the fabricated bow-tie PCA and detected by the fabricated spiral PCA (a) time-domain and (b) frequency-domain responses

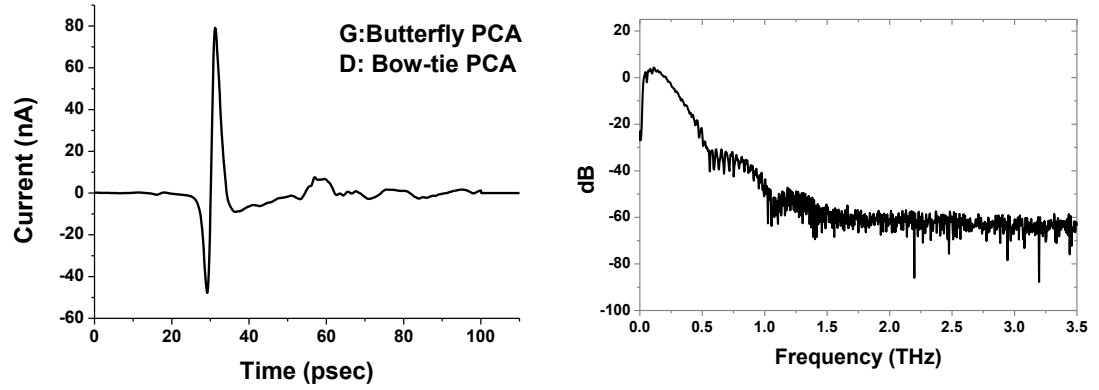


(a) (b)

Figure 5.5 The THz signal generated by the fabricated butterfly PCA and detected by the fabricated spiral PCA (a) time-domain and (b) frequency-domain responses

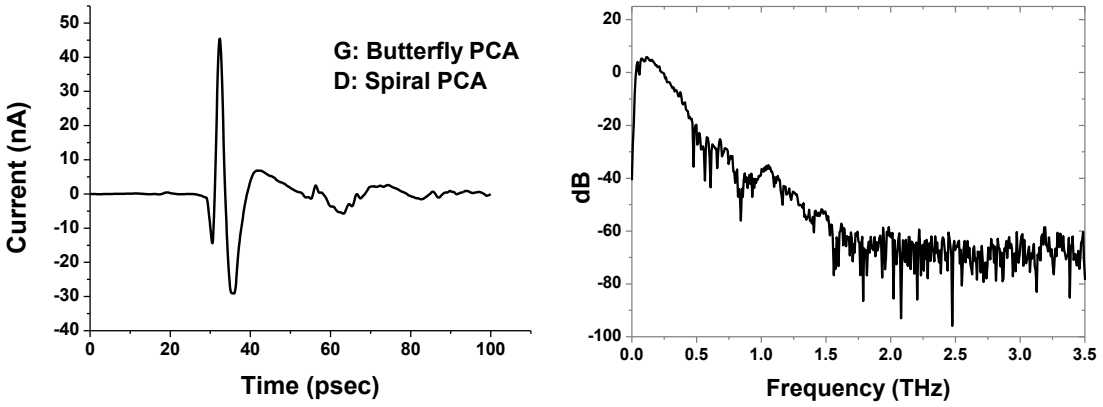
5.1.2 Testing the THz-PCAs as THz Detectors

THz detectors are important components that affect the performance of the imaging and spectroscopy systems; hence, the fabricated spiral, bow-tie and butterfly PCAs are tested as THz detectors using the commercial BATOP butterfly PCA as a THz source. The detected THz signals are represented in both the time- and frequency-domains in Figure 5.6 to Figure 5.8.



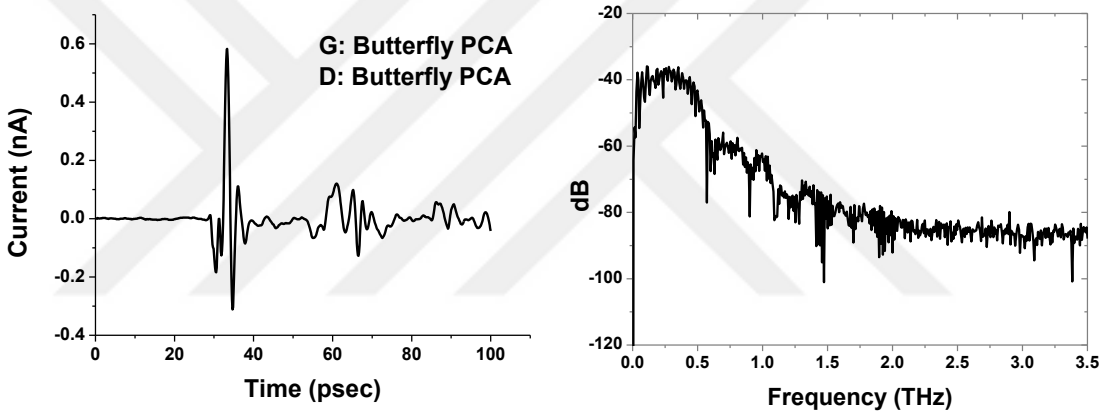
(a) (b)

Figure 5.6 The THz signal detected by the fabricated bow-tie PCA and generated by the commercial butterfly PCA (a) time-domain and (b) frequency-domain responses



(a) (b)

Figure 5.7 The THz signal detected by the fabricated spiral PCA and generated by the commercial butterfly PCA (a) time-domain and (b) frequency-domain responses



(a) (b)

Figure 5.8 The THz signal detected by the fabricated butterfly PCA and generated by the commercial butterfly PCA (a) time-domain and (b) frequency-domain responses

5.2 Time-Domain Radiation Pattern Characterization

To substantiate the proposed method, the THz peak positions that occur due to the new optical path lengths for each radiation pattern measurement point in the lateral dimension on E- and H- planes are measured. Then, the shifts on the optical delay line are compared with the THz peak positions shifts that are calculated using equation 1, and the results are given in Figure 5.9 to Figure 5.12. The manual adjustment of the transitional stage yields some error between the measurements and calculations. Figure 5.13 to Figure 5.16 represent the error analysis of the shifted

positions of the maximum THz signals, where the maximum errors for the peak shifts comparison are 8%, 4%, 2% and 4% for the dipole, spiral, bow-tie, and butterfly PCAs, respectively. The error results show that the measured THz peak positions shifts are in a good agreement with the calculated shifts.

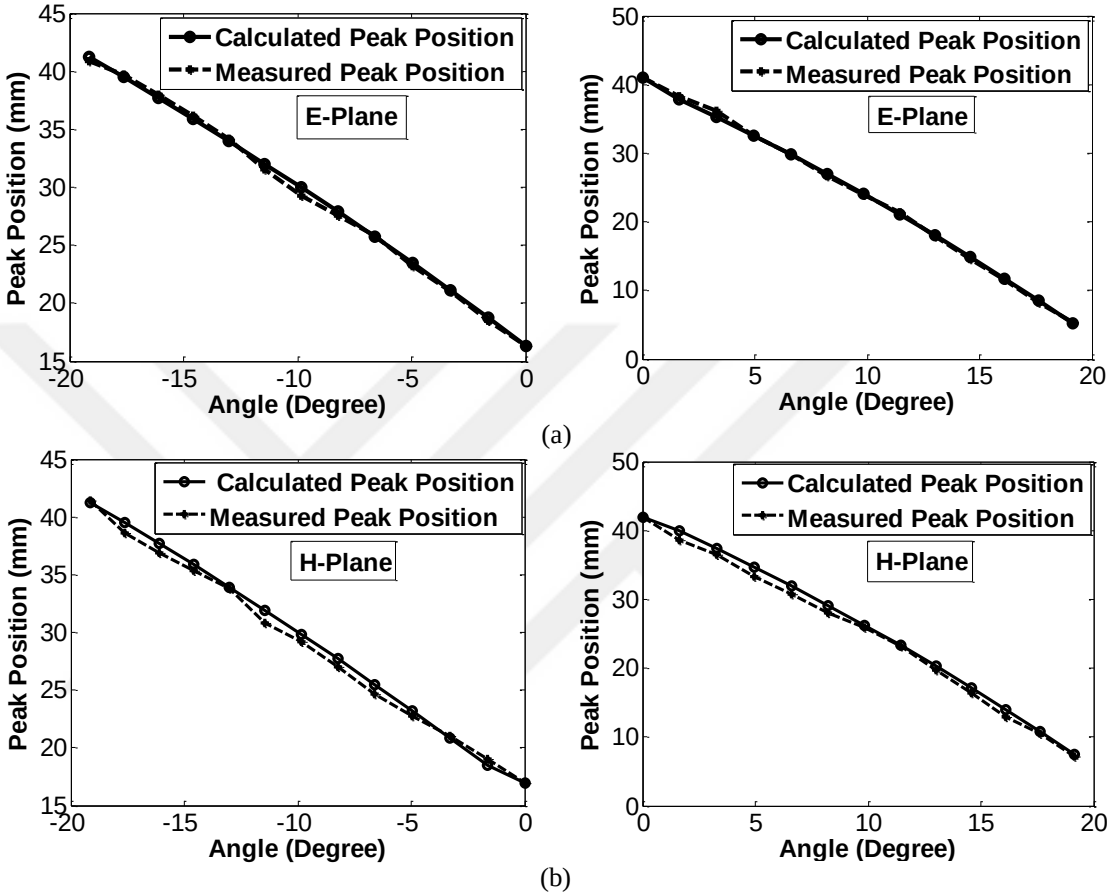


Figure 5.9 The measured and calculated the max. THz signal shifted positions of the dipole PCA for the negative (LHS) and positive (RHS) transitional stage movement directions (a) E-plane and (b) H-plane

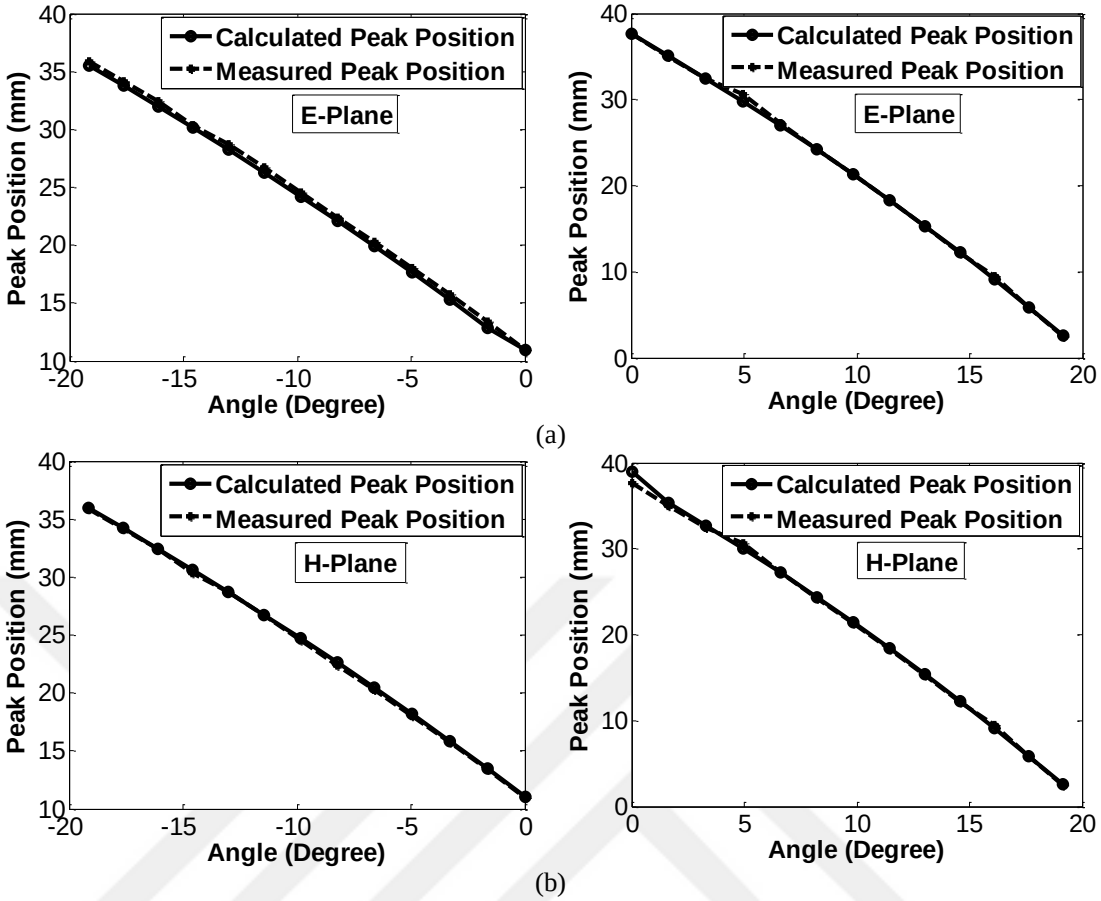
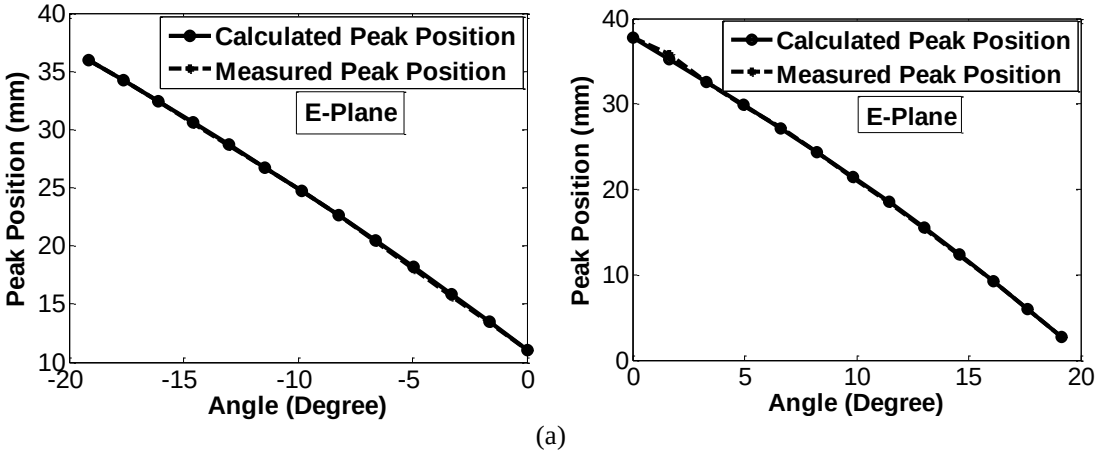
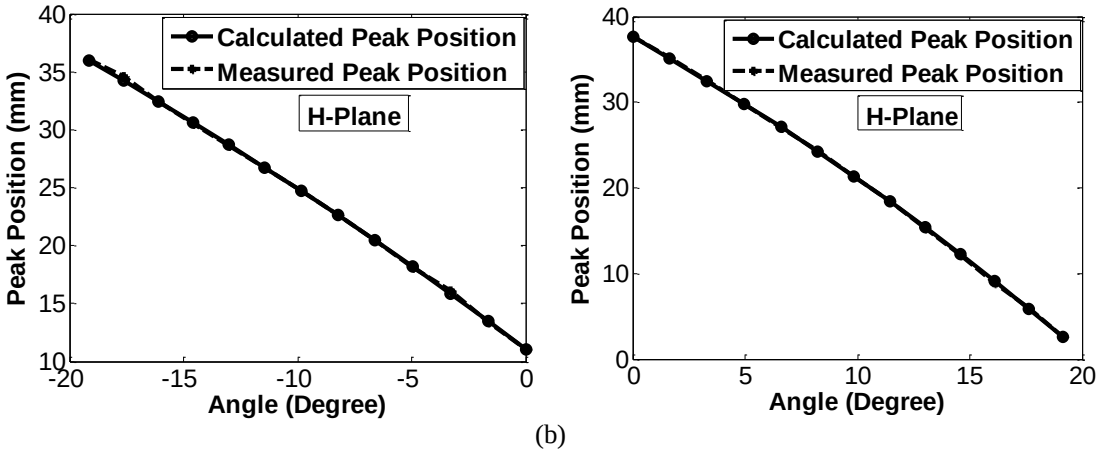


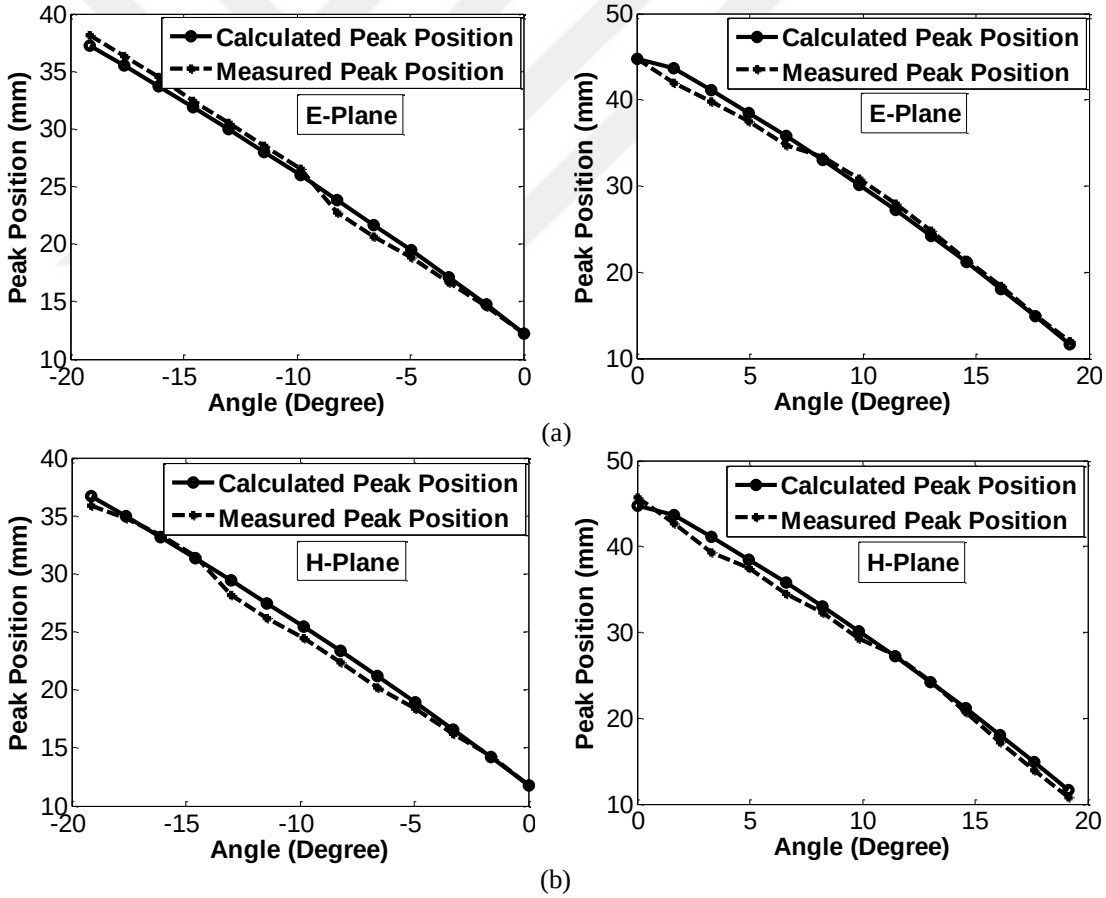
Figure 5.10 The measured and calculated the max. THz signal shifted positions of the spiral PCA for the negative (LHS) and positive (RHS) transitional stage movement directions (a) E-plane and (b) H-plane





(b)

Figure 5.11 The measured and calculated the max. THz signal shifted positions of the bow-tie PCA for the negative (LHS) and positive (RHS) transitional stage movement directions (a) E-plane and (b) H-plane



(a)

(b)

Figure 5.12 The measured and calculated the max. THz signal shifted positions of the butterfly PCA for the negative (LHS) and positive (RHS) transitional stage movement directions (a) E-plane and (b) H-plane

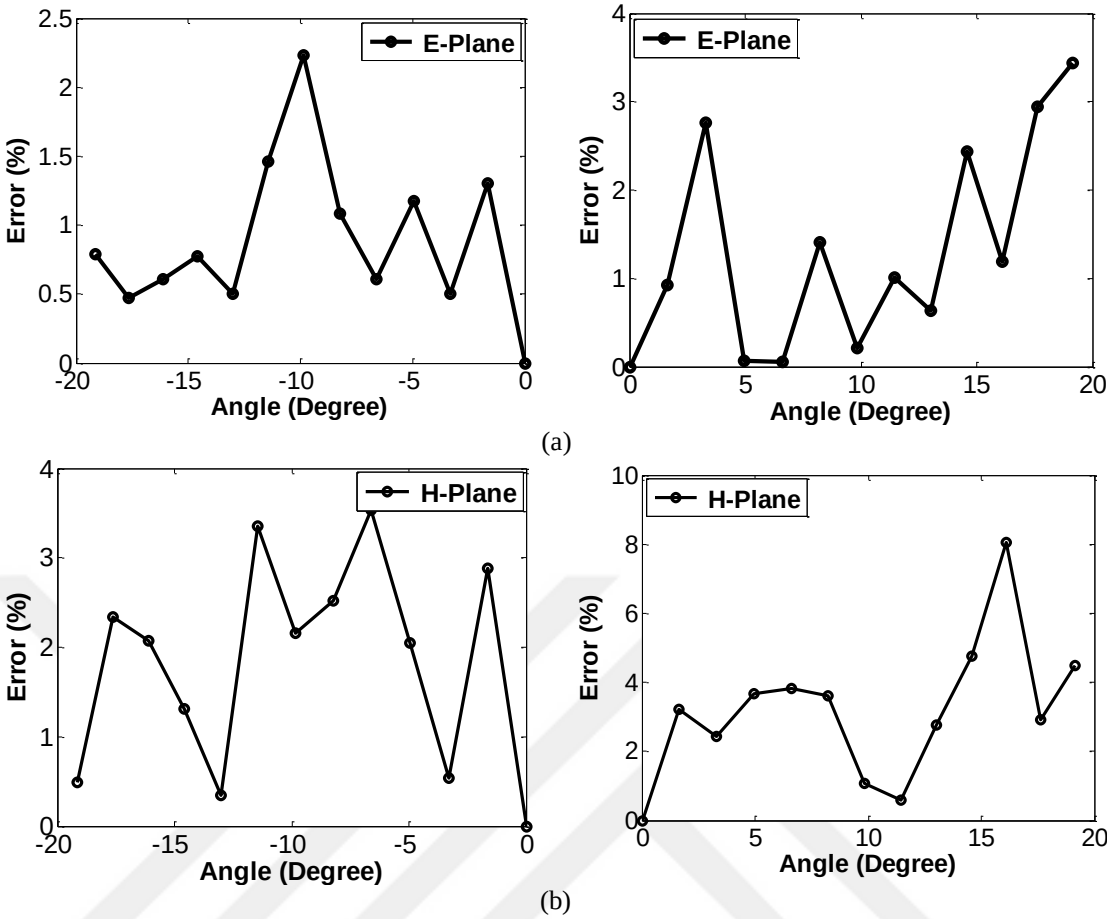
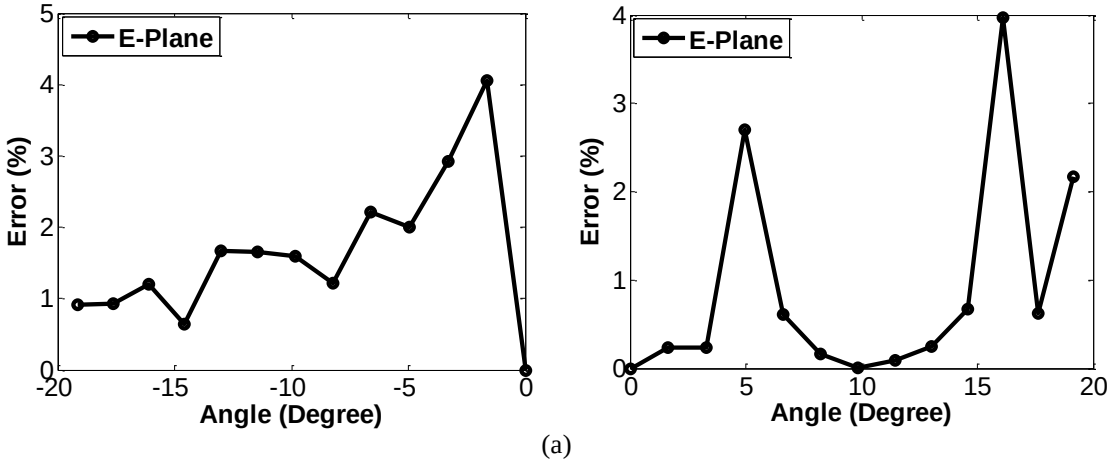
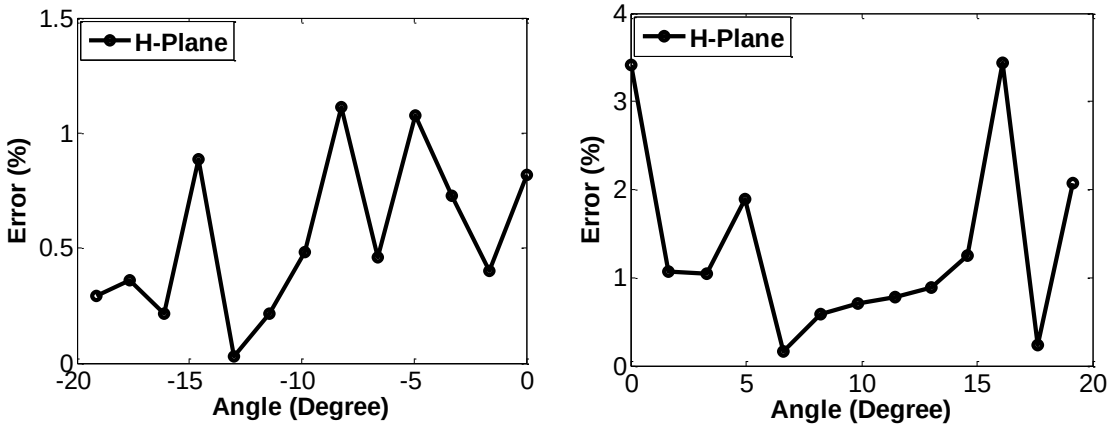


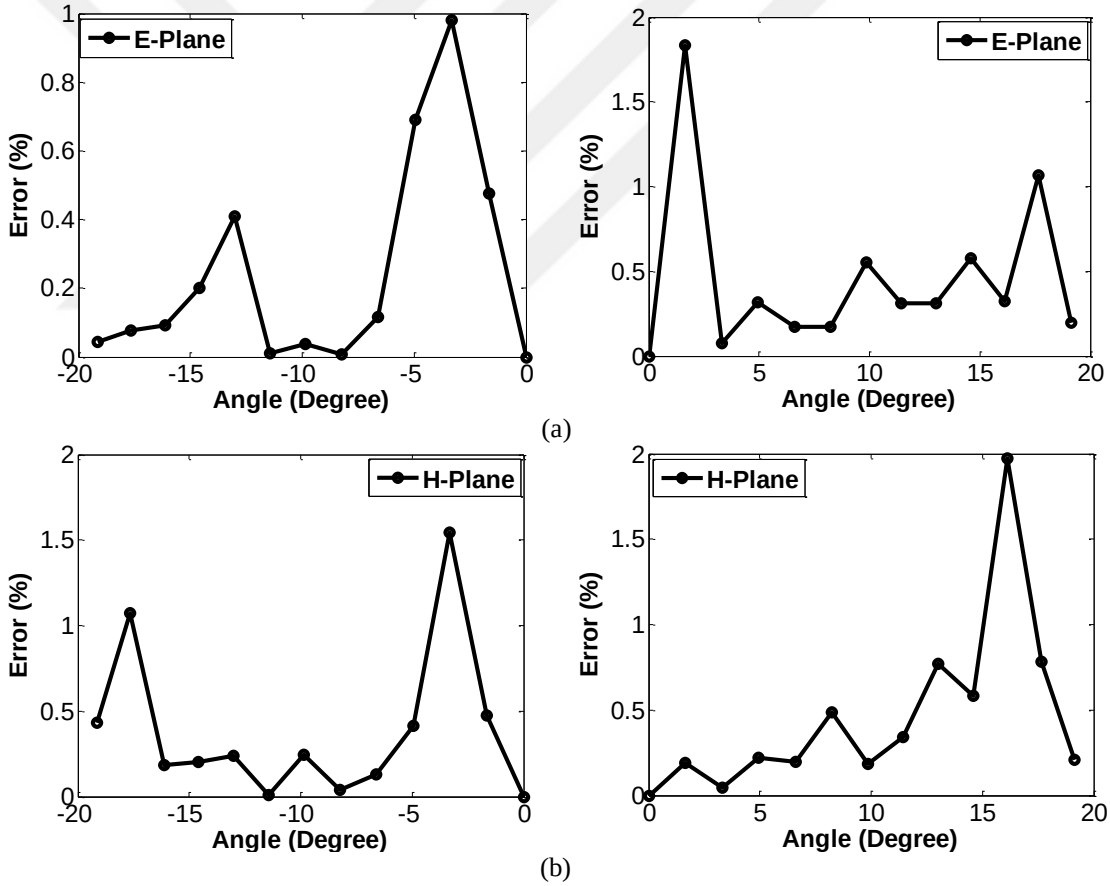
Figure 5.13 The error analysis of the max. THz signal shifted positions of the dipole PCA for the negative (LHS) and positive (RHS) movement directions (a) E-plane and (b) H-plane





(b)

Figure 5.14 The error analysis of the max. THz signal shifted positions of the spiral PCA for the negative (LHS) and positive (RHS) movement directions (a) E-plane and (b) H-plane



(a)

(b)

Figure 5.15 The error analysis of the max. THz signal shifted positions of the bow-tie PCA for the negative (LHS) and positive (RHS) movement directions (a) E-plane and (b) H-plane

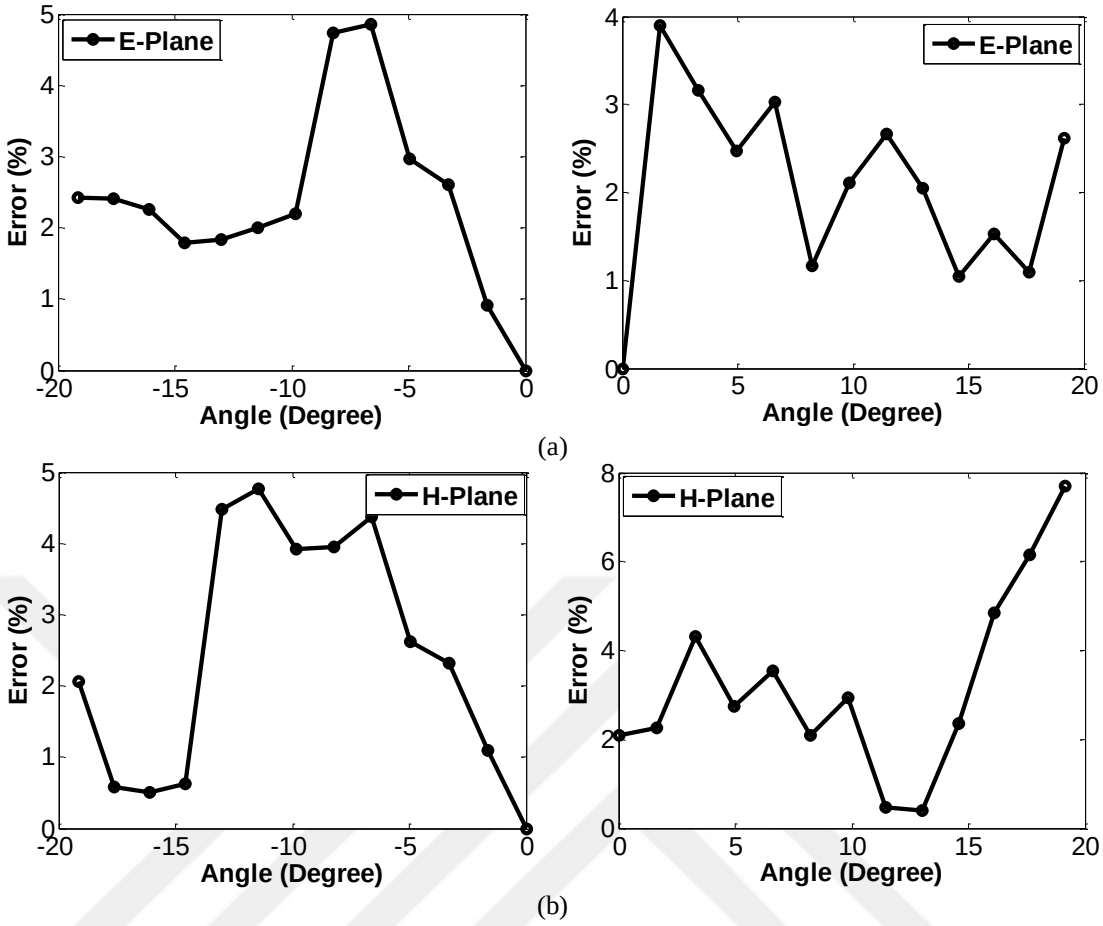
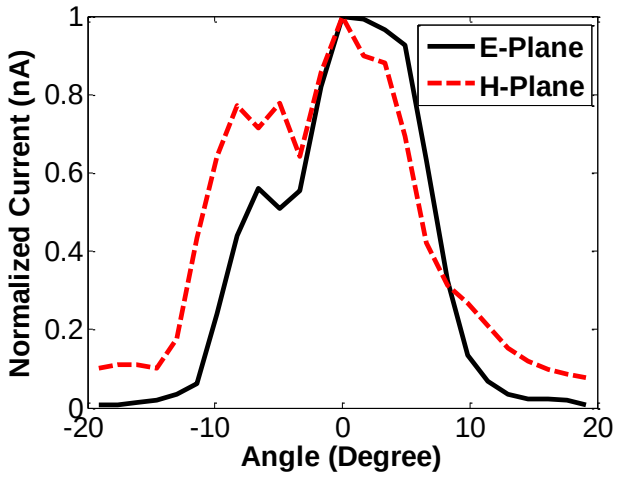
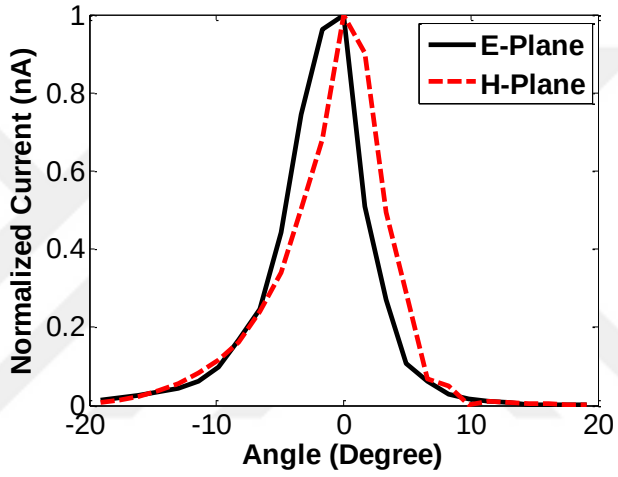


Figure 5.16 The error analysis of the max. THz signal shifted positions of the butterfly PCA for the negative (LHS) and positive (RHS) movement directions (a) E-plane and (b) H-plane

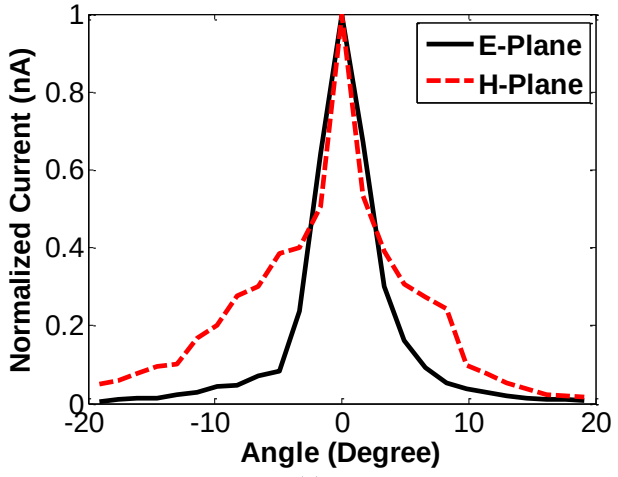
The two-dimensional spatial distribution of the THz signal generated by the characterized THz-PCA is obtained by measuring the maximum of the time-domain THz signal at each measurement position. The measurements are taken with a step size of 5 mm, in the range of ±60 mm that corresponds to ±19.1° with respect to the position of the PCA under test. The measurements of the normalized far-field radiation pattern of the characterized PCAs are shown in Figure 5.17.


E-Plane
H-Plane
Normalized Current (nA)
Angle (Degree)
0
0.2
0.4
0.6
0.8
1
-20
-10
0
10
20

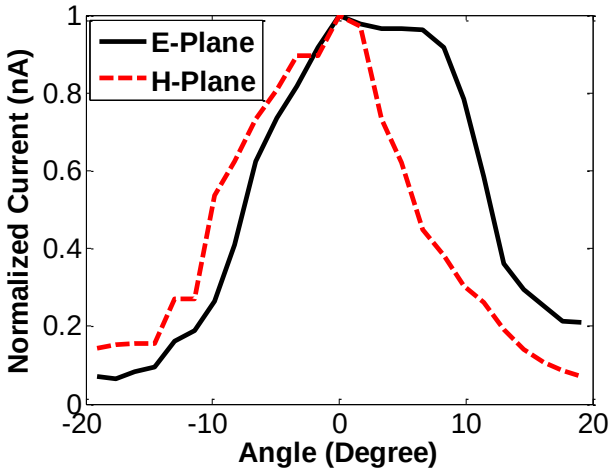
(a)


E-Plane
H-Plane
Normalized Current (nA)
Angle (Degree)
0
0.2
0.4
0.6
0.8
1
-20
-10
0
10
20

(b)


E-Plane
H-Plane
Normalized Current (nA)
Angle (Degree)
0
0.2
0.4
0.6
0.8
1
-20
-10
0
10
20

(c)



(d)

Figure 5.17 The normalized measured time-domain radiation pattern of the (a) commercial dipole, (b) spiral, (c) bow-tie and (d) butterfly characterized THz-PCAs

To verify the proposed method, the radiation pattern of the characterized PCAs is also examined using numerical calculations where the CST environment is used. Each of the PCAs is simulated together with the silicon lens in time-domain, the detection PCA in the proposed modified THz-TDS is represented by the probe in the CST environment. By moving the probe in the lateral dimension, running the simulation, and recording the maximum of the time-domain probe signal at each measurement position the far-field radiation pattern of the PCAs is obtained. The simulation results are compared with the measured radiation patterns as indicated in Figure 5.18 to Figure 5.21.

The differences in the half-power beam width (HPBW) between the measurement and simulation results are calculated as 1 and 3.2° for the dipole PCA, 1.64 and 1.65° for the spiral PCA, 1.65 and 1.6° for the bow-tie PCA, and 0.8 and 0.9° for the butterfly PCA in the E-plane and H-plane, respectively. Bearing in mind these results, there exist asymmetrical behaviors of the radiation patterns of the butterfly and dipole PCAs. This is basically a result of the DC bias line disturbances of the PCA emission properties, which considerably affect the radiation characteristics of the PCA. On the other hand, the spiral and bow-tie PCAs have shown a lower asymmetrical behavior on their radiation patterns. This result is expected due to the optimization procedure of the DC bias lines placement in order to minimize their

effect on the radiation properties. In the simulations, the DC bias lines effects are also observed. To reduce the simulation complexity the DC bias lines connections are cut out at some point, hence, their effects are less dominantly observed. Nevertheless, the measurement and simulation results clearly show that the spatial emission distribution can be different than the ideal situation and should be taken into account for the accurate characterization of the terahertz signals.

The proposed setup is a free-space modified THz-TDS thus small degrees of tilting errors are results of the THz-PCAs alignment. These tilting errors are corrected as -1° for the E-plane radiation pattern of the dipole PCA, -1 and +0.6° for E-plane and H-plane radiation patterns of the spiral PCA, respectively, -0.9 and -1° for E-plane and H-plane radiation patterns of the bow-tie PCA, respectively, and -3° for E-plane radiation pattern of the butterfly PCA.

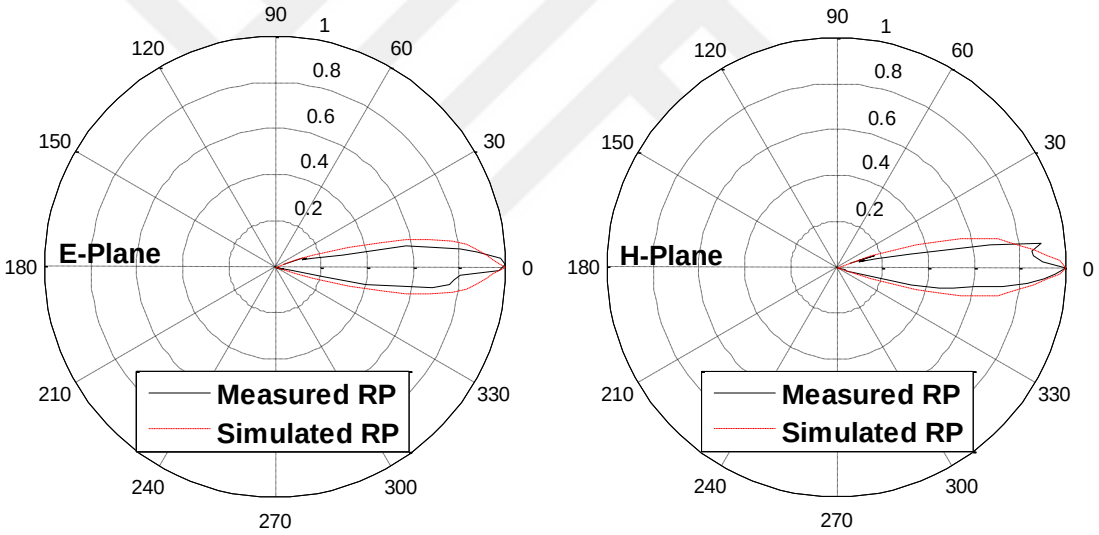
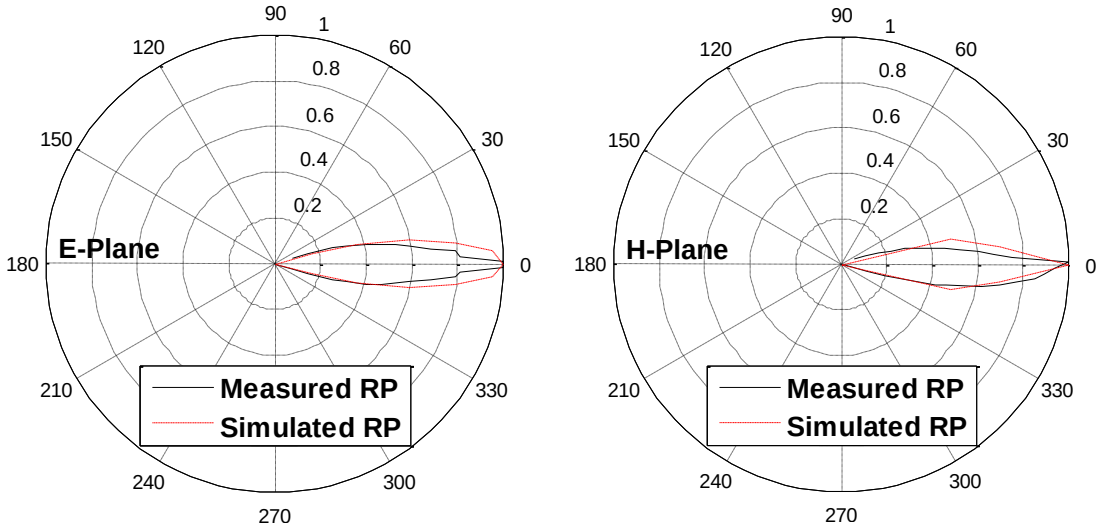
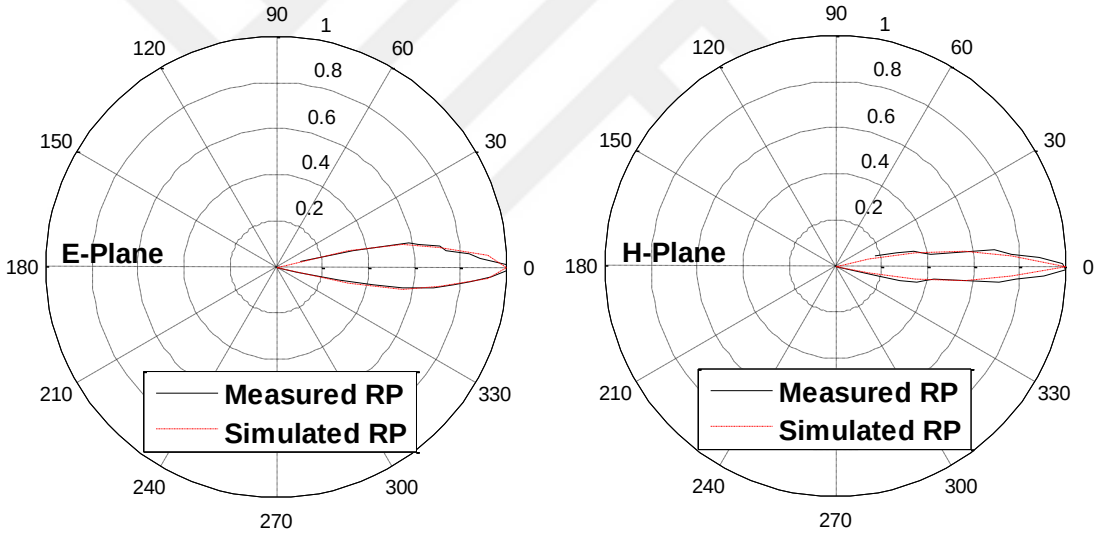


Figure 5.18 The radiation Pattern (RP) of the dipole PCA (a) E-plane and (b) H-plane



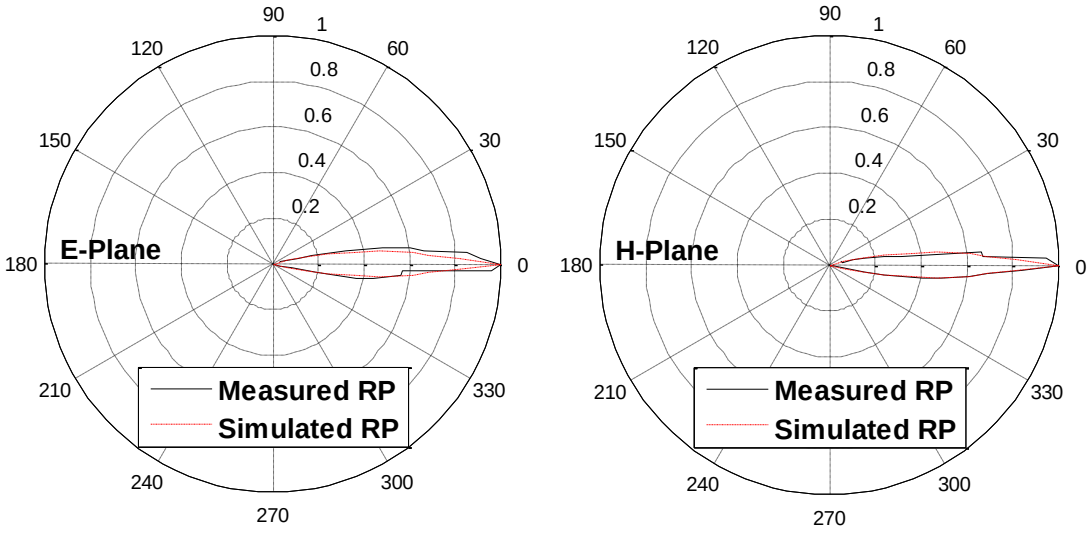
(a) (b)

Figure 5.19 The radiation Pattern (RP) of the spiral PCA (a) E-plane and (b) H-plane



(a) (b)

Figure 5.20 The radiation Pattern (RP) of the bow-tie PCA (a) E-plane and (b) H-plane



(a) (b)

Figure 5.21 The radiation Pattern (RP) of the butterfly PCA (a) E-plane and (b) H-plane

5.3 THz Beam-Steering Array Characterization

The proposed modified THz-TDS setup is used to characterize the THz beam-steering array that is designed to steer the THz beam 3°. The radiation pattern of the array is characterized in the range of ±8°. First, the array is characterized to make sure that the beam is steered in the direction of the stubs as in the configuration in Figure 5.22. The comparison of the measured and calculated maximum THz signal shifted positions for the array radiation pattern characterization is illustrated in Figure 5.23. The radiation pattern of the array is characterized with a maximum error of 0.8% as illustrated in Figure 5.24. The radiation pattern of the array is shown in Figure 5.25 and Figure 5.26 where it can be clearly observed that the array steered the THz signal -3.31°, the minus sign indicates that the THz signal is steered in the direction of the subs when the array is characterized in the configuration in Figure 5.22.

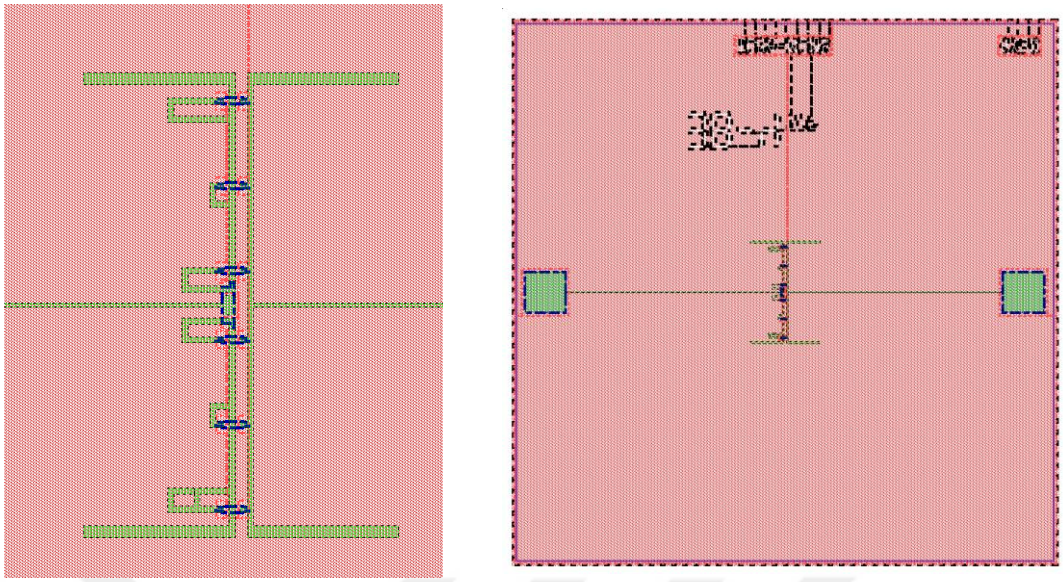


Figure 5.22 Beam-steering array layout [Designed by Kazim Demir]

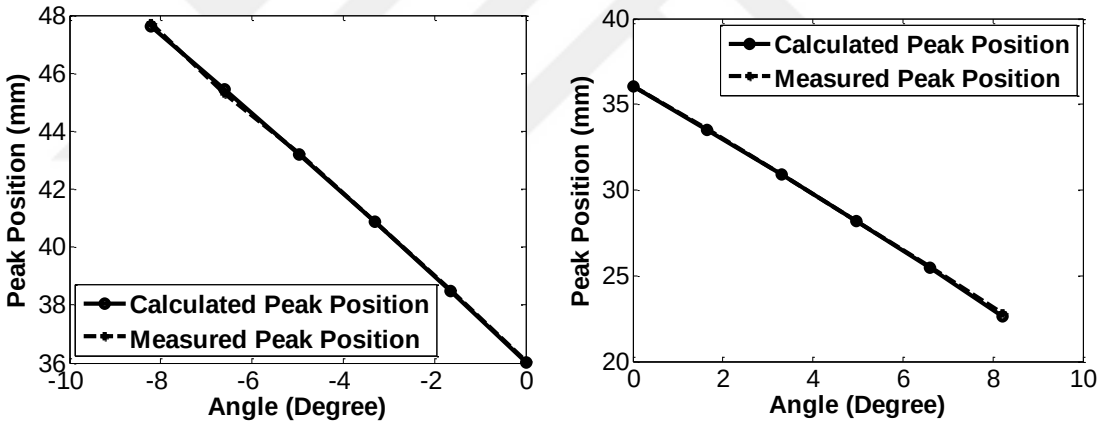


Figure 5.23 The measured and calculated the max. THz signal shifted positions of the beam-steering array for the negative (LHS) and positive (RHS) transitional stage movement directions

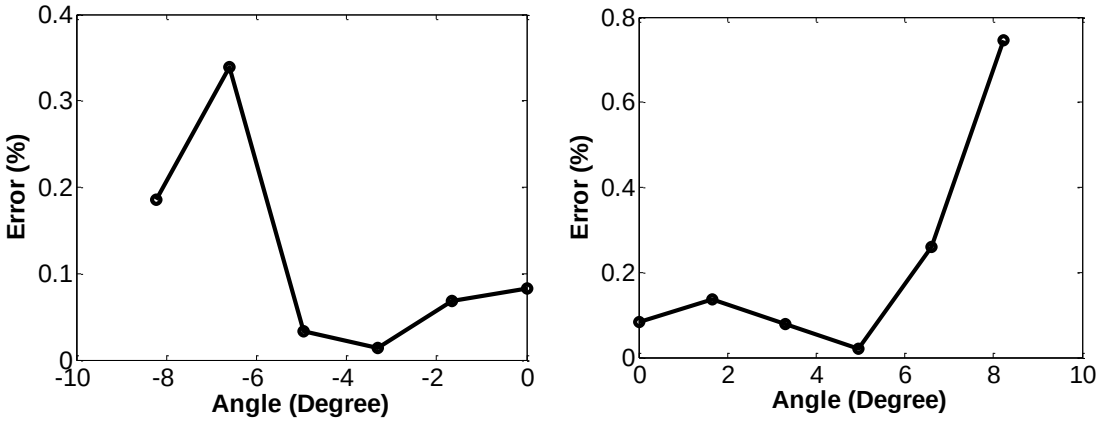


Figure 5.24 The error analysis of the max. THz signal shifted positions of the beam-steering array for the negative (LHS) and positive (RHS) movement directions

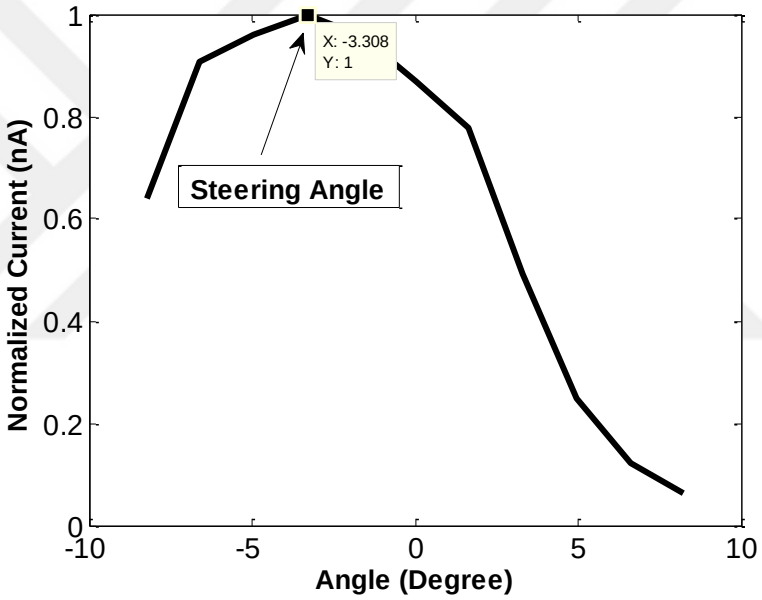


Figure 5.25 The normalized measured time-domain radiation pattern of the beam steering array

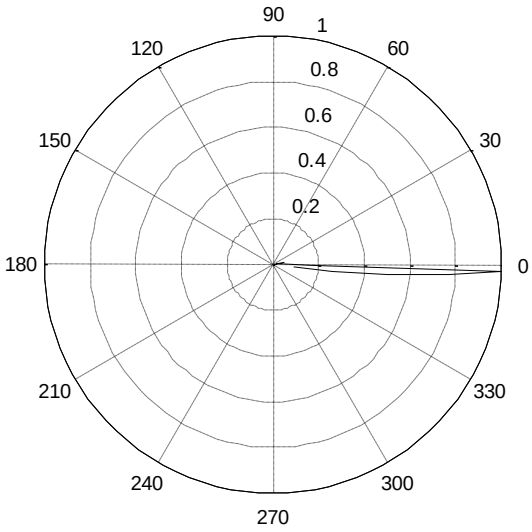
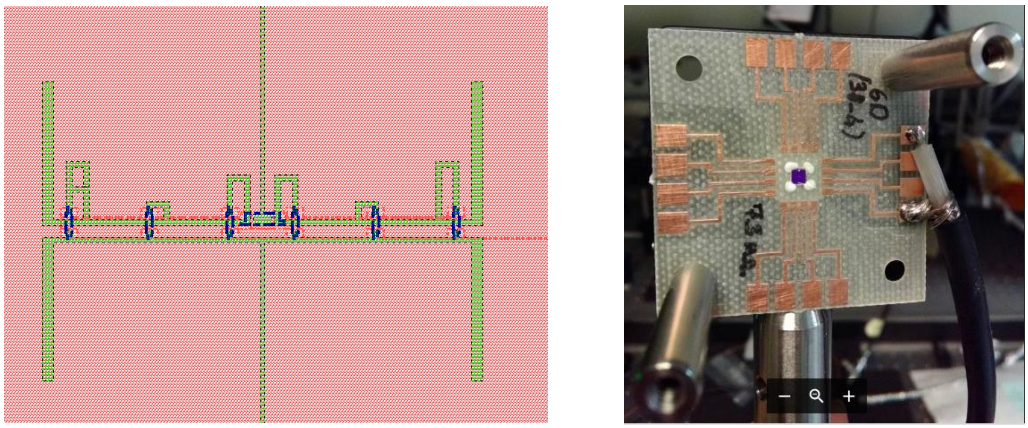


Figure 5.26 Radiation Pattern of the beam-steering array

The characterized array is designed to steer the THz beam in the in the direction of the stubs as in the configuration in Figure 5.27. The comparison of the measured and calculated maximum THz signal shifted positions for the array radiation pattern characterization is illustrated in Figure 5.28. The radiation pattern of the array is characterized with a maximum error of 1.65% as illustrated in Figure 5.29. The normalized measured time-domain radiation pattern of the array is plotted in Figure 5.30 where it can be clearly observed that the array steered the THz signal 3.31° in the direction of the longest sub when the array is characterized in the configuration in Figure 5.27. The polar plot of the steered radiation pattern in illustrated is Figure 5.31.



(a) (b)

Figure 5.27 Beam-steering array (a) layout [Designed by Kazim Demir] (b) photograph

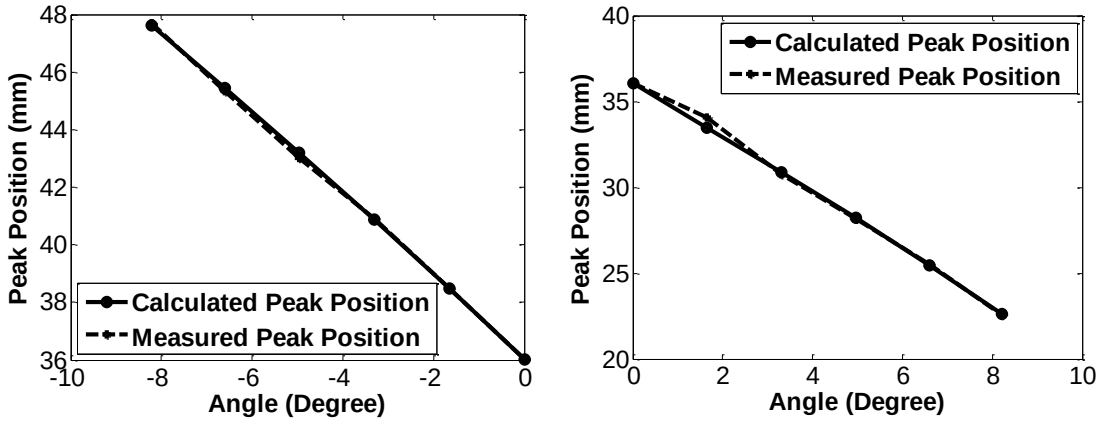


Figure 5.28 The measured and calculated the max. THz signal shifted positions of the beam-steering array for the negative (LHS) and positive (RHS) transitional stage movement directions

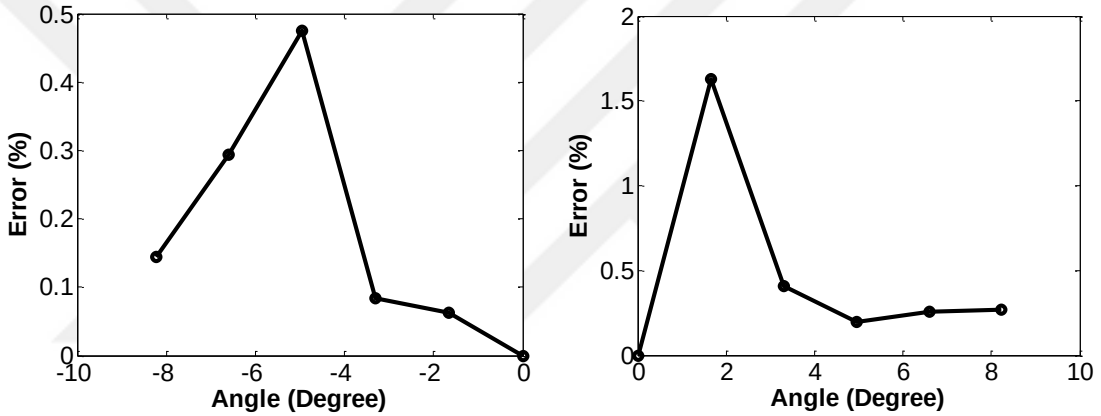


Figure 5.29 The error analysis of the max. THz signal shifted positions of the beam-steering array for the negative (LHS) and positive (RHS) movement directions

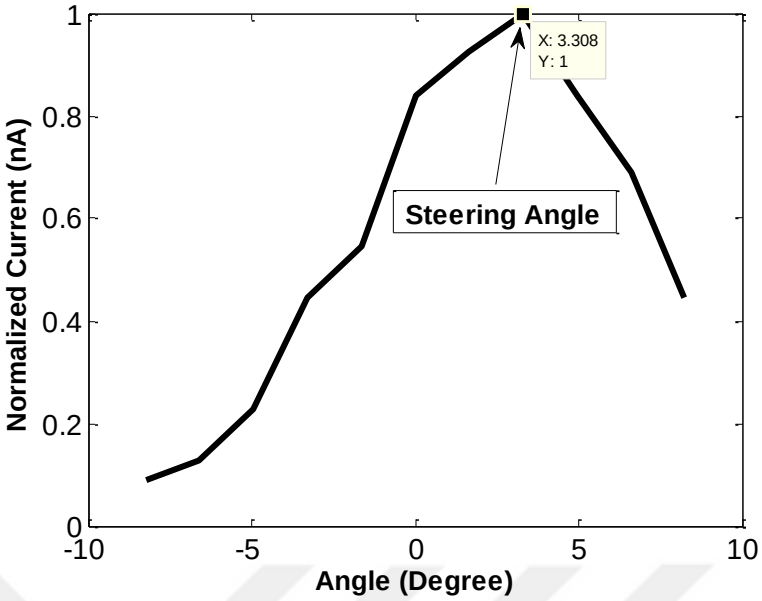


Figure 5.30 The normalized measured time-domain radiation pattern of the beam steering array

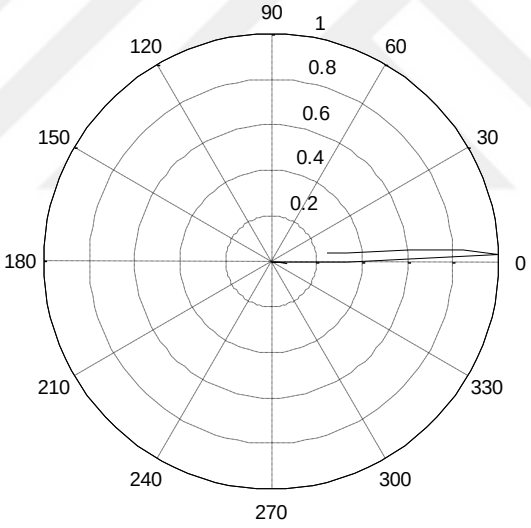


Figure 5.31 The radiation Pattern of the beam-steering array

CHAPTER 6

CONCLUSIONS AND SUGGESTIONS

In this dissertation, the main focus is on the development of THz-TDS systems for the time-domain characterization of THz-PCAs and beam-steering arrays. Moreover, testing and characterizing the designed and fabricated THz-PCAs and beam-steering arrays.

A novel technique to characterize the time-domain radiation pattern of the LT-GaAs based THz-PCAs in the two major radiation planes is proposed. This technique is applied to characterize the beam-steering arrays and the THz-PCAs, namely spiral, dipole, butterfly, and bow-tie PCAs. The proposed method is successful for the time-domain radiation pattern characterization of the THz-PCAs and beam-steering arrays due to he good agreement that is observed by comparing the measured results with the analytical calculations and the simulation results clearly shows that The measurements of the time-domain radiation pattern of the THz-PCAs and beam steering arrays show that they should be taken into account to improve the performance of the THz-TDS systems.

The characterization of the THz-PCAs and antenna arrays in time-domain is critical in the pulsed THz-TDS systems that are used in ultra-wideband applications. In THz-TDS systems, the time-domain radiation pattern characterization of the THz-PCAs, as well as beam-steering arrays, is as much important as the single frequency characterization due to the fact that for ultra-wideband frequency response the THz-TDS systems use pulsed THz signals, and the single frequency characterization provides limited information regarding the behavior of the THz-PCAs. As the fact that, in ultra-wideband applications where pulsed THz-TDS systems have the advantage to provide more useful information than the CW-THz systems, the dominant peak height vs. position plays a significant role in the measurements which is not obtainable in the single frequency responses. The proposed modified THz-TDS system can be very advantageous for the development of THz optical systems since it

can improve the THz signal level substantially and compensate the errors that caused by the radiation characteristics of the THz-PCA in the system.

Consequently, the time-domain measurements will play a substantial role in the performance improvement of the next-generation THz imaging, spectroscopy, security, and high-speed communication systems, where the THz-PCAs will be implemented in large-scale arrays. Accordingly, to improve the performance of the proposed technique and to characterize a higher angular range of the radiation pattern a higher travel range motorized linear translation stage is suggested to be used. Moreover, the setup will be improved to characterize the 2D radiation patterns that are important in imaging and security applications especially when the system is designed based on antenna arrays. A circular scanning of the time-domain radiation pattern will be implemented to reduce the off-axis error and to improve the setup for the characterization of other types of THz-PCAs. The superposition method will be improved by taking into account the effects of the antenna at each single frequency in the broadband range.

REFERENCES

[1] Popovic, Z. & Grossman, E. N. THz Metrology and Instrumentation. IEEE Transactions on Terahertz Science and Technology. (1). (1) 133-144. 2011

[2] Armstrong, C. M. The Truth about Terahertz. IEEE Spectrum. 36-41. 2012

[3] Siegel, P. H. THz Technology: An Overview. International Journal of High Speed Electronics and Systems. (13). (2) 351-394. 2003

[4] Lee, Y.-S. *Principles of Terahertz Science and Technology*. Springer. New York. ISBN 978-0-387-09539-4. 2009

[5] Ferguson, B. & Zhang, X. Materials for Terahertz Science and Technology. Nature Materials. (1) 26-33. 2002

[6] Burforda, N. M. & El-Shenaweeb. M. O. Review of terahertz photoconductive antenna technology. Optical Engineering. (56). (1) 010901-1-010901-20. 2017

[7] Choudhury, B. Sonde, A. & Jha, R. M. Terahertz Antenna Technology for Space Applications. Springer. Singapore. ISBN 978-981-287-799-4. 2016

[8] Smith, R. & Arnold, M. Terahertz Time-Domain Spectroscopy of Solid Samples: Principles, Applications, and Challenges. Applied Spectroscopy Reviews. (46) 636–679. 2011

[9] Auston, D. H. Cheung, K. P. & Smith, P. R. Picosecond photoconducting Hertzian dipoles. Applied Physics Letters. (45). (3) 284–286. 1984

[10] Perenzoni, M. Paul, D. J. *Physics and Applications of Terahertz Radiation*. Springer. ISSN 1556-1534. 2014

[11] Lewis, R. A. A review of terahertz sources. J. Phys. D: Appl. Phys. (47) 1-11. 2014

[12] Zhang, X.C. & Xu, J. *Introduction to THz Wave Photonics*. Springer. New York. ISBN 978-1-4419-0977-0. 2010

[13] Angrisani, L. Cavallo, G. Liccardo, A. Papari, G. P. & Andreone. A. *THz Measurement Systems*. Chapter. DOI:10.5772/63734. 2016

[14] Akyildiz, F. Jornet, J. M. & Hana, C. Terahertz band: Next frontier for wireless communications. Physical Communication. (12). 16–32. 2014

[15] Topical Review. The 2017 terahertz science and technology roadmap. J. Phys. D: Appl. Phys. (50), 043001. 2017.

[16] Pawar, A. Y. Sonawane, D. D. Erande, K. B. & Derle, D. V. Terahertz technology and its applications. Drug Invention Today. (5), 157-163. 2013

[17] Nanophotonics and Terahertz Technology (NTT) group a part of the Chair of Photonics in the Institute for Microwave Engineering and Photonics (IMP). https://www.imp.tu-darmstadt.de/forschung_imp/ont_imp/ntt.de.jsp. May 2019

[18] Kürner, T. & Priebe, S. Towards THz Communications - Status in Research, Standardization and Regulation. J Infrared Milli Terahz Waves. DOI 10.1007/s10762-013-0014-3. 2013

[19] Ho, L. Pepper, M, & Taday, P. Terahertz spectroscopy Signatures and fingerprints. Nature Photonics. (2) 541-543. 2008

[20] Redo-Sanchez, A. Laman, N. Schulkin, B. & Tongue, T. Review of Terahertz Technology Readiness Assessment and Applications. J Infrared Milli Terahz Waves. DOI:10.1007/s10762-013-9998-y. 2013

[21] Tonouchi, M. Cutting-edge terahertz technology. Nature Photonics. (1) 97-105. 2007

[22] Bowman, T. El-shenawee, M. & Campbell, L. K. Terahertz transmission vs. reflection imaging and model-based characterization for excised breast carcinomas. Biomedical Optics Express. (7). (9) 3756-3783. 2016

[23] Woolard, D. L. Brown, E. R. Pepper, M. & Kemp M. Terahertz Frequency Sensing and Imaging: A Time of Reckoning Future Applications? Proceedings of the IEEE. (93). (10) 1722-1743. 2005

[24] Kamburoğlu, K. Karagöz, B. Altan, H. & Özen, D. An Ex vivo Cmparative Study of Occlusal and Proximal Caries Using Terahertz and X-ray Imaging. Dentomaxillofac Radiol. (47) 20180250. 2018

[25] Karagöz, B. Altan, H. & Kamburoğlu, K. Terahertz Pulsed Imaging Study of Dental Caries. Proc. of SPIE-OSA. (9542) 95420N-1-95420N-8. 2015

[26] Haaser, M. Gordon, K. C. Strachan, C. J. & Rades, T. Terahertz pulsed imaging as an advanced characterization tool for film coatings-A review. International Journal of Pharmaceutics. (457) 510– 520. 2013

[27] Karpowicz, N. Zhong, H. Xu, J. Lin, K. Hwang, J. S. & Zhang, X. C. Comparison between Pulsed Terahertz Time-domain Imaging and Continuous Wave Terahertz Imaging. Semiconductor Science and Technology. (20) S293–S299. 2005

[28] O'Sullivan, C. & Murphy, J. A. Field Guide to Terahertz Sources, Detectors, and Optics. SPIE. 2012

[29] Gallerano, G. P. & Biedron, S. Overview of Terahertz Radiation Sources. Proceedings of the FEL Conference, 216-221. 2004

[30] Sakai, K. *Terahertz Optoelectronics*. Springer. New York. ISSN 0303-4216. 2005

[31] Tani, M. Hirota, Y. Que, C. T. Tanaka, S. Hattori, R. Yamaguchi, M. Nishizawa, S. Hangyo, M. Novel Terahertz Photoconductive Antennas. International Journal of Infrared and Millimeter Waves. (27). (4) 531-546. 2006

[32] Jepsen, P. U. Jacobsen, R. H. & Keiding. S. R. Generation and detection of terahertz pulses from biased semiconductor antennas. J. Opt. Soc. Am. B. (13). (11) 2424-2436. 1996

[33] Preu, S. Döhler, G. H. Malzer, S. Wang, L. J. & Gossard, A. C. Tunable, Continuous-wave Terahertz Photomixer Sources and Applications. Journal of Applied Physics, 109. 061301. 2011

[34] Berry, C. W. Wang, N. Hashemi, M. R. Unlu, M. & Jarrahi, M. Significant performance enhancement in photoconductive terahertz optoelectronics by incorporating plasmonic contact electrodes. Nature Communications. DOI: 10.1038/ncomms2638. 2013

[35] Jepsen, P. U., Cooke, D. G., & Koch, M. Terahertz spectroscopy and imaging–Modern techniques and applications. Laser Photonics Rev. (5), (1) 124-166. 2011

[36] Liu, H. B. Zhong, H. Karpowicz, N. Chen, Y. & Zhang, X. C. Terahertz Spectroscopy and Imaging for Defense and Security Applications. Proceedings of the IEEE. (95). (8) 1514-1527. 2007

[37] Zhang, T. Zhang, Z. & Arnold, M. A. Polarizability of Aspirin at Terahertz Frequencies Using Terahertz Time Domain Spectroscopy (THz-TDS). Applied Spectroscopy. 2019. DOI: 10.1177/0003702818815177.

[38] Ye, H. M. Li, H. & Yao, S.F. Characterizing the Structure and Phase Transformation of Poly(ethylene Oxide)–Urea Complexes Using Terahertz Time-Domain Spectroscopy. Applied Spectroscopy. (71). (11) 2549-2554. 2017

[39] Yu, C. Fan, S. Sun, Y. & Pickwell-MacPherson, E. The Potential of Terahertz Imaging for Cancer Diagnosis: A review of investigations to date. Quantitative Imaging in Medicine and Surgery. (2). (1) 33-45. 2012

[40] Tonouchi, M. Galore New Applications of Terahertz Science and Technology. Terahertz Science and Technology (2). (3) 90-101. 2009

[41] Mendis, R. Sydlo, C. Sigmund, J. Feiginov, M. Meissner, P. & Hartnagel, H. L. Spectral Characterization of Broadband THz Antennas by Photoconductive Mixing: Toward Optimal Antenna Design. IEEE Antennas and Wireless Propagation Letters. (4) 85-88. 2005

[42] Lepeshov, S. Gorodetsky, A. Krasnok, A. Rafailov, E. & Belov, P. Enhancement of Terahertz Photoconductive Antenna Operation by Optical Nanoantennas. Laser Photonics Rev. DOI: org/10.1002/lpor.201600199. 2016

[43] Computer Simulation Technology (https://www.cst.com/). 2019

[44] Zomega Terahertz Corporation. *The Terahertz Wave eBook*. Technical Overview. 2012

[45] Adam, A. J. L. Review of Near-Field Terahertz Measurement Methods and Their Applications. J Infrared Milli Terahz Waves. (32) 976–1019. 2011

[46] Wahaia, F, Kašalynas, I. Valušis, G. Carvalho Silva G., C. D & Granja, P. L. Terahertz Spectroscopy for Gastrointestinal Cancer Diagnosis. *Terahertz Spectroscopy - A Cutting Edge Technology*. Chapter 13, 247-266. DOI: http://dx.doi.org/10.5772/66999. 2017

[47] Gowen, A. A. O'Sullivan, C. & O'Donnell, C. P. Terahertz time domain spectroscopy and imaging: Emerging techniques for food process monitoring and quality control. Trends in food Science & Technology. (25) 40-46. 2012

[48] Naftaly, M. & Miles, R. E. Terahertz Time-Domain Spectroscopy for Material Characterization. Proceedings of the IEEE. (95). (8) 1685-1665. 2007

[49] Withayachumnankul, W. & Naftaly. M. Fundamentals of Measurement in Terahertz Time-Domain Spectroscopy. J Infrared Milli Terahz Waves. (35) 610–637. 2014

[50] Hou, L. & Shi, W. An LT-GaAs Terahertz Photoconductive Antenna with High Emission Power, Low Noise, and Good Stability. IEEE Transactions on Electron Devices. (60). (5) 1619-1624. 2013

[51] Zhang, J. Tuo, M. Liang, M. Ng, W. Gehm, M. E. & Hao Xin, M. E. Terahertz Emission Properties of Butterfly-shaped Photoconductive Antennas Based on LT-GaAs and SI-GaAs Substrates. IEEE-ISAPE2012. DOI: 10.1109/ISAPE.2012.6408990. 2012

[52] Huang, Z. Yu, B. Zhao, G. Zhang, C. Cui, L. & Li, Y, Study on Terahertz Emission Properties of Bow-Tie Photoconductive Antenna. Proceedings of SPIE. 7158: 715812-1- 715812-10. 2008

[53] Yandong, G. Hui, D. & Paulose, V. Simple Methods to Measure Partial Polarization Parameters in the Terahertz Band Using THz-TDS. Microwave and optical technology letters. (52). (9). 2010

[54] Watanabe, S. Yasumatsu, N. Oguchi, K. Takeda, M. Suzuki, T. & Tachizaki, T. A Real-Time Terahertz Time-Domain Polarization Analyzer with 80-MHz Repetition-Rate Femtosecond Laser Pulses. Sensors. (13) 3299-3312. 2013

[55] Dickhoff, R. Jastrow, C. Steiger, A. Müller, R. Kleine-Ostmann T. & T. Schrader. Characterization of THz Beams. OSA/ CLEO 2011

[56] Molloy, J. F. Naftaly, M. & Dudley, R. A. Characterization of Terahertz Beam Profile and Propagation. IEEE Journal of Selected Topics in Quantum Electronics. (19). (1) DOI:10.1109/JSTQE.2012.2205668. 2013

[57] Tiedje, H. F. Saeedkia, D. Nagel, M. & Haugen, H. K. Optical Scanning Techniques for Characterization of Terahertz Photoconductive Antenna Arrays. IEEE Transactions on Microwave Theory and Techniques. (58). (7) 2040-2045. 2010

[58] Shams, M. I. B. Jiang, Z. Qayyum, J. Rahman, S. M. Xing, H.G. Hesler, J. L. et. al. Characterization of Terahertz Antennas Using Photoinduced Coded-Aperture Imaging. Microwave and Optical Technology Letters. (57). (5) 1180-11842015. 2015

[59] Jepsen, P. U. & Keiding, S. R. Radiation patterns from lens-coupled terahertz antennas. Optics Letters. (20). (8) 807-809. 1995

[60] Tani, M. Matsuura, S. Sakai, K. & Nakashima, S. Emission characteristics of photoconductive antennas based on low-temperature-grown GaAs and semi-insulating GaAs. Applied Optics. (36). (30) 7853-7859. 1997

[61] Neu, J. & Schmuttenmaer C. A. Tutorial: An Introduction to Terahertz Time Domain Spectroscopy (THz-TDS). Journal of Applied Physics. (124) 231101-1-231101-14. 2018

[62] Rudd, J. & Mittleman, D. Influence of substrate-lens design in terahertz time-domain spectroscopy. J. Opt. Soc. Am. B. (19). (2) 319-329. 2002

[63] Grischkowsky, D. Keiding, S. Exter, M. V. & Fattinger, C. Far-infrared Time-domain Spectroscopy with Terahertz Beams of Dielectrics and Semiconductors. J. Opt. Soc. Am B. (7). (10) 2006-2015. 1990

[64] Filipovic, D. F. Gauthier, G. P. Raman, S. & Rebeiz, G. M. Off-Axis Properties of Silicon and Quartz Dielectric Lens Antennas. IEEE Transactions on Antennas and Propagation. (45). (5) 760-766. 1997

[65] Elmabruk, K. Demir, K. Sahin, A. B. Altan, H. & Unlu, M. Radiation Pattern Characterization of Terahertz Photoconductive Antennas Using Time-Domain Spectroscopy System. 2018 IEEE International Symposium on Antennas and Propagation and USNC-URSI Radio Science Meeting, Boston, MA, USA. 8-13. 2018.

[66] Elmabruk, K. Demir, K. Altan, H. Sahin, A. B. & Unlu, M. Time-Domain Characterization of the Radiation Pattern of the Terahertz Photoconductive Antennas. Journal of Infrared, Millimeter, and Terahertz Waves. (6). (40). DOI: 10.1007/s10762-019-00588-y. 2019

[67] Celik, S. B. Demir, K. Sahin, A. B. & Unlu, M. Design of a Phase Shifting Impedance Tuner for Terahertz Photomixers Arrays. IEEE AP-S 2017. 1281-1282. 2017

[68] Celik, S. B. Demir, K. Sahin, A. B. & Unlu, M. Design of a Terahertz Beam-Steering Photomixer Array. IEEE AP-S 2017. 303-304. 2017

[69] BATOP GmbH (https://www.batop.de/). 2019

[70] Balanis, C. A. *Antenna Theory Analysis and Design*. John Wiley & Sons, Inc. Hoboken, New Jersey. ISBN: 0-471-66782-X. 2005

[71] MATLAB - MathWorks - MATLAB & Simulink (https://www.mathworks.com/products/matlab.html). 2019

[72] High-Frequency Structure Simulator (HFSS) (https://www.ansys.com/products/electronics/ansys-hfss). 2019

CURRICULUM VITAE

PERSONAL INFORMATION

Name Surname: Kholoud ELMABRUK

Date of Birth: 30/12/1984

Phone: +90 541 726 97 16

E-mail: kholoudelmabruk@gmail.com

EDUCATION

High School: (1998-2001) Al qudus High School, Gharian/Libya.

Bachelor: (2001-2006) Electrical and electronic engineering dep. "Communication", Aljabal Algarbi University, Gharian/Libya, (79.22/100).

Master Degree: (2010-2012) Communication and electronic engineering dep./ Çankaya University, Ankara/Turkey, (3.81/4.00).

WORK EXPERIENCE

- (2008-2009): research assistance at Aljabal Algarbi University, Garian/ Libya.

Courses taught:

  - Basics of electronic circuits.
  - Analog electronic circuits.
  - Signals and systems.

- 2006-2007: trainee at OXY petroleum ltd, Tripoli/ Libya.

PUBLICATIONS:

Journal Publications - Peer-review:

- ***Kholoud Elmabruk,*** Halil Eyyuboglu, “Analysis of Flat-Topped Gaussian Vortex Beam Scintillation Properties in Atmospheric Turbulence”. Optical Engineering. 58(6). DOI: 10.1117/1.OE.58.6.066115. 2019
- ***Kholoud Elmabruk***, Kazim Demir, Asaf Bahzit Sahin, Hakan Altan, Mehmet Unlu, “Time-Domain Characterization of the Radiation Pattern of the Terahertz Photoconductive Antennas”. Journal of Infrared, Millimeter, and Terahertz Waves. DOI: 10.1007/s10762-019-00588-y. 2019
- Ali Haider, Petro Deminskyi, Mehmet Yilmaz, ***Kholoud Elmabruk***, Ibrahim Yilmaz, Necmi Biyikli, “Long-range ordered vertical III-nitride nanocylinder arrays via plasma-assisted atomic layer deposition”. J. Mater. Chem. C. (6) 6471-6482. 2018

Conference Proceedings:

- ***Kholoud Elmabruk***, Kazim Demir, Asaf Bahzit Sahin, Hakan Altan, Mehmet Unlu, “Radiation Pattern Characterization of Terahertz Photoconductive Antennas Using Time-Domain Spectroscopy System”. 2018 IEEE International Symposium on Antennas and Propagation and USNC-URSI Radio Science Meeting, Boston, MA, USA. 8-13. (2018).
- Ali Haider, Petro Deminskyi, ***Kholoud Elmabruk***, Sevde Altuntas, Ibrahim Yilmaz, Fatih Buyukserin, Necmi Biyikli, “Low-Temperature Conformal Growth of Ordered III-nitride and Metal-Oxide Hollow Nanocylinder Arrays for Optoelectronics and Photocatalytic”, MRS Fall Meeting, Boston, Massachusetts, 27 November – 2 December (2016).
- Ibrahim Yilmaz, ***Kholoud Elmabruk***, Ali Haider, Sevde Altuntas, Fatih Buyukserin, Necmi Biyikli, “Temperature-dependent photoluminescence characteristics of plasmaassisted ALD-grown ordered GaN nanostructures on Si substrates”, 16th International Conference on Atomic Layer Deposition (ALD 2016), Dublin, Ireland, 24 – 27 July (2016).
- Ali Haider, Cagla Ozgit-Akgun, ***Kholoud Elmabruk***, Ibrahim Yilmaz, Necmi Biyikli, “Template Assisted Growth of GaN Nanostructures by Hollow Cathode Plasma-assisted Atomic Layer Deposition”, 15th International Conference on Atomic Layer Deposition (ALD 2015), Portland, OR. 28 June – 2 July (2015)

Projects:

- "Beam steering, frequency reconfigurable terahertz photomixer array using nano-actuators". Funded by: EU H2020 Marie Sklodowska Curie Program, Reintegration (RI) Grant.
- "Development of frequency reconfigurable, wideband, high radiation resistance photomixers and photoconductive antennas for terahertz frequencies (114E089)". Funded by: TUBITAK (3501).

Skills:

Languages:

- Arabic "Native"
- English "advanced"
- Turkish "basics"

Computer:

- ICDL "International computer driving license"
- MATLAB
- Origin
- CST
- HFSS